

# Flow splitting in numerical simulations of oceanic dense-water outflows



Gustavo M. Marques<sup>a,\*</sup>, Mathew G. Wells<sup>b</sup>, Laurie Padman<sup>c</sup>, Tamay M. Özgökmen<sup>d</sup>

<sup>a</sup> Atmospheric and Oceanic Sciences Program, Princeton University, Princeton, New Jersey, USA

<sup>b</sup> Department of Physical and Environmental Sciences, University of Toronto Scarborough, Toronto, Canada

<sup>c</sup> Earth and Space Research, Corvallis, Oregon, USA

<sup>d</sup> Rosenstiel School of Marine and Atmospheric Science, University of Miami, Miami, Florida, USA

## ARTICLE INFO

### Article history:

Received 12 September 2016

Revised 11 March 2017

Accepted 19 March 2017

Available online 25 March 2017

### Keywords:

Intermediate and bottom water formation

Internal hydraulic jump

Overflows

Gravity currents

## ABSTRACT

Flow splitting occurs when part of a gravity current becomes neutrally buoyant and separates from the bottom-trapped plume as an interflow. This phenomenon has been previously observed in laboratory experiments, small-scale water bodies (e.g., lakes) and numerical studies of small-scale systems. Here, the potential for flow splitting in oceanic gravity currents is investigated using high-resolution ( $\Delta x = \Delta z = 5 \text{ m}$ ) two-dimensional numerical simulations of gravity flows into linearly stratified environments. The model is configured to solve the non-hydrostatic Boussinesq equations without rotation. A set of experiments is conducted by varying the initial buoyancy number  $B_0 = Q_0 N^3 / g'$  (where  $Q_0$  is the volume flux of the dense water flow per unit width,  $N$  is the ambient stratification and  $g'$  is the reduced gravity), the bottom slope ( $\alpha$ ) and the turbulent Prandtl number ( $Pr$ ). Regardless of  $\alpha$  or  $Pr$ , when  $B_0 \leq 0.002$  the outflow always reaches the deep ocean forming an underflow. Similarly, when  $B_0 \geq 0.13$  the outflow always equilibrates at intermediate depths, forming an interflow. However, when  $B_0 \sim 0.016$ , flow splitting always occurs when  $Pr \geq 10$ , while interflows always occur for  $Pr = 1$ . An important characteristic of simulations that result in flow splitting is the development of Holmboe-like interfacial instabilities and flow transition from a supercritical condition, where the Froude number ( $Fr$ ) is greater than one, to a slower and more uniform subcritical condition ( $Fr < 1$ ). This transition is associated with an internal hydraulic jump and consequent mixing enhancement. Although our experiments do not take into account three-dimensionality and rotation, which are likely to influence mixing and the transition between flow regimes, a comparison between our results and oceanic observations suggests that flow splitting may occur in dense-water outflows with weak ambient stratification, such as Antarctic outflows.

© 2017 Elsevier Ltd. All rights reserved.

## 1. Introduction

Oceanic outflows are large-scale density-driven currents generated either at high latitudes, where water density increases due to cooling and brine rejection from growing sea ice, or in subtropical marginal seas, where water density increases due to evaporation. These outflows have been widely studied (Legg et al., 2009; Price and Baringer, 1994), since they play an important role in establishing the large-scale circulation. In general, high latitude outflows, e.g. Denmark Strait outflow (Girton and Sanford, 2003), Faroe Bank Channel outflow (Mauritzen et al., 2005) and Antarctic outflows (Foldvik et al., 2004; Gordon et al., 2004; Muench et al., 2009), sink to the bottom of their respective basins, while outflows located

closer to the equator, e.g., Mediterranean Sea outflow (Baringer and Price, 1997; Price et al., 1993) and Red Sea outflow (Matt and Johns, 2007; Peters et al., 2005), equilibrate at intermediate depths.

There is no clear observational evidence that major oceanic outflows, such as those discussed by Price and Baringer (1994) and Legg et al. (2009), can vertically split into two or more branches as a consequence of mixing and affect intermediate and deep layers simultaneously.<sup>1</sup> Nevertheless, flow splitting in smaller scale density-driven currents has been observed in lakes (De Cesare et al., 2006), in a Mediterranean reservoir (Cortés et al., 2014a) and in the Arctic Ocean (Aagaard et al., 1985). Given the difficulties in measuring oceanic outflows, especially at high latitudes,

<sup>1</sup> The Mediterranean outflow splits into two cores after the flow begin to descend into the Gulf of Cadiz, but this is a consequence of topographic steering (Baringer and Price, 1997). In the present work, focus is given to flow splitting induced by mixing rather than topographic effects.

\* Corresponding author.

E-mail address: [gmarques@princeton.edu](mailto:gmarques@princeton.edu) (G.M. Marques).

and the fact that there are many processes acting in these flows concurrently (e.g., tides, hydraulic control, thermobaric effect and geostrophic eddies), it is possible that flow splitting could also take place in large-scale oceanic outflows but has not been identified. If that is the case, conceptual models developed to close the heat budget in the global overturning circulation (Hughes and Griffiths, 2006; Wählín and Cenedese, 2006; Wells and Wettlaufer, 2007) would have to be revisited, since they assume that large-scale high-latitude oceanic outflows only ventilate the abyssal ocean. Throughout this paper, we follow the terminology used by limnologists and classify the different flow regimes as interflow, underflow or split flow.

Much of what is known about dense outflows comes from numerous laboratory experiments of bottom gravity currents (Baines, 2001, 2005; Cenedese et al., 2004; Cenedese and Adduce, 2008; Cortés et al., 2014b; Ellison and Turner, 1959; Lane-Serff and Baines, 1998; Mitsudera and Baines, 1992; Monaghan, 2007; Simpson, 1999; Wells and Wettlaufer, 2007; Wells and Nadarajah, 2009). Ellison and Turner (1959) proposed a theory for the bulk properties of a density gravity current flowing into homogeneous ambient water. They showed that the entrainment velocity of the plume ( $W_e$ ) could be represented as the product of the mean fluid velocity ( $U$ ) and an entrainment parameter ( $E$ ) that is an empirical function of the Richardson number ( $Ri$ ) for the layer. Cenedese et al. (2004) added the effects of a rotating tank and found the development of three flow regimes (laminar, waves and eddies), where each of them has different mixing characteristics. In a follow-up study, Cenedese and Adduce (2008) showed that  $E$  also depends on the Reynolds number ( $Re$ ), and not just on  $Ri$  as previously proposed by Ellison and Turner (1959).

For non-rotating gravity currents flowing down slopes and into linearly stratified environments, Mitsudera and Baines (1992) showed the development of a well-defined turbulent layer with up- and downslope streaming formed above the bottom current. These experiments also revealed the presence of cusp-shaped waves near the top of the slope, which were attributed to generation of Holmboe-like instabilities. Baines (2001) then proposed that these instabilities are responsible for the wisps of detrained fluid observed in laboratory experiments. These observations highlighted the different characteristics of the flow compared with experiments with homogeneous ambient stratification, and motivated additional laboratory experiments by Baines (2005, 2008). In the latter, ranges of ambient stratification frequencies ( $N$ ) and slope angles ( $\theta$ ) were used and two main types of flow regimes emerged: 1) for sufficiently large  $\theta$ , the flow was dominated by strong entrainment balanced by buoyancy force; and 2) for small  $\theta$ , the flow detrained and the balance was mainly controlled by buoyancy force and bottom drag. Herein, we use  $\alpha = \tan(\theta)$  to represent the slope of  $\theta$ .

An additional flow regime, characterized by the splitting of the gravity current and the presence of both entrainment and detrainment, was also observed by Baines (2005, 2008) (Fig. 1), but it was not explored in detail and remains unexplained in continuously stratified environments. These different flow regimes were investigated in the context of a non-dimensional parameter, namely the initial buoyancy number ( $B_0$ ):

$$B_0 = \frac{Q_0 N^3}{g_0^2}, \quad (1)$$

where  $g'_0$  is the reduced gravity ( $g'_0 = g \frac{\Delta\rho}{\rho_0}$ ),  $Q_0$  is the volume flux of the dense water per unit width at the top of the slope,  $g$  is the acceleration due to gravity,  $\Delta\rho$  is the density difference between the outflow and the environmental fluid just above it, and  $\rho_0$  is a reference density.

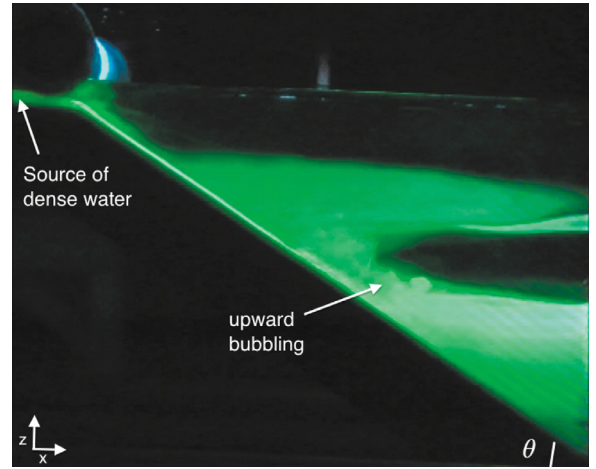


**Fig. 1.** An example of flow splitting observed in a non-rotating laboratory experiment where dense water flows down on a steep shelf slope ( $\theta = 30^\circ$ ) and into a linearly stratified ambient water (adapted from Baines, 2008). The fluid has been dyed with fluorescence and is illuminated by a thin laser beam that scans a central vertical section.

The flow splitting regime shown in Fig. 1 was observed in just two experiments with a very large angle ( $\theta = 30^\circ$ ) and with intermediate values of  $B_0$  ( $1.7$  and  $4.0 \times 10^{-3}$ ). It is characterized by the splitting of the main plume into two branches: a denser and less diluted plume at the bottom, and a less dense and more diluted plume located at intermediate depths.

Density flows can also be studied in numerical models. Guo et al. (2014) conducted numerical simulations of non-rotating laboratory-scale gravity currents descending a slope into a linearly stratified environment. Based on front positions, density and vertical velocity profiles, they showed that their simulations were in good agreement with laboratory experiments (Baines, 2001, 2005; Mitsudera and Baines, 1992). However, Guo et al. (2014) did not explore the flow splitting regime since their simulations were only run for a short time and just one of their experiments showed the beginning of a split scenario with blobs of dense water detaching from the main current (see their Figs. 3c and d). While there have been some numerical studies investigating flow splitting in two-layer systems (Cortés et al., 2015; Wobus et al., 2013), this type of flow has never been modeled in detail in a linearly stratified environment.

Additional insights can be gained from studies based on non-rotating laboratory experiments of dense water flowing down slopes into a two-layered ambient stratification (Cortés et al., 2014b; Monaghan, 2007; Wells and Wettlaufer, 2007). Three possible outcomes have been described for this setup (see Figs. 1a, b and c in Cortés et al., 2014b): 1) the flow separates from the bottom and forms an interflow; 2) the flow reaches the bottom of the domain and forms an underflow; or 3) the flow splits as it impinges into the single density step and forms two intrusions. The latter is the equivalent to the flow splitting in a linearly stratified environment shown in Fig. 1.

Motivated by observational evidence of flow splitting in a Mediterranean reservoir, Cortés et al. (2014b) conducted a series of laboratory experiments to investigate the splitting of a gravity current upon reaching a density interface. These authors proposed that flow splitting can be predicted based upon two non-dimensional parameters: the density Richardson number ( $Ri_\rho$ ) and the densimetric Froude number ( $Fr$ ). These numbers are defined as:

$$Ri_\rho = \frac{g'_{12} h_1}{B_f^{2/3}}, \quad (2)$$

and

$$Fr = \frac{U}{\sqrt{g'h}} \quad (3)$$

where  $g'_{12} = g(\rho_2 - \rho_1)/\rho_1$  is the reduced gravity of the ambient water density step;  $\rho_1$  and  $\rho_2$  are the densities of the upper and lower layer, respectively;  $h_1$  is the thickness of the upper layer;  $B_f = g(\rho_0 - \rho_1)Q_0/(\rho_1 W)$  is the inflow buoyancy flux;  $\rho_0$  and  $W$  are the initial density and width of the outflow, respectively;  $U$  is the mean bottom current speed; and  $h$  is the outflow thickness. For  $Ri_\rho$  in the range  $5 \leq Ri_\rho \leq 40$ , flow splitting was more likely to occur as the density interface of the gravity current became more diffusive (i.e., when  $Fr > 1$ ). In a follow-up study, Cortés et al. (2015) performed numerical simulations to further explore the behavior of a gravity current in a two-layer system. They found good agreement between simulations and laboratory experiments, and confirmed the importance of the internal properties of the gravity current in determining the different flow regimes.

The fate of dense outflows in nature is expected to depend on the shear and density gradient at the plume's interface (i.e.,  $Fr$ ) and the resulting turbulence (i.e.,  $Re$ ) (e.g., Girton and Sanford, 2003). Thus, to apply the results from laboratory experiments to geophysical flows these parameters must be similar. In laboratory experiments, turbulence can only be generated by using slope angles much larger than those observed in nature. Otherwise, the density current cannot accelerate within the bounds of typical laboratory tanks [ $O(1)$  m] and the flow is not turbulent. Even when large slope angles are used in laboratory studies,  $Re$  is still orders of magnitude smaller than in geophysical flows (e.g., Baines, 2001). Therefore, it is not known whether the results from laboratory experiments discussed above remain valid for geophysical parameters and scales.

Since some realistic parameters cannot be reproduced in the laboratory, numerical simulations have been used to complement our understanding of the dynamics of bottom density currents from a geophysical point of view (e.g., Ezer, 2005; Jackson et al., 2008; Legg et al., 2006; 2009; Özgökmen and Chassignet, 2002; Özgökmen et al., 2004, 2006; Özgökmen and Fischer, 2008; Wobus et al., 2013). The two-dimensional (2D) non-hydrostatic simulations presented by Özgökmen and Chassignet (2002) captured qualitatively the major features of bottom gravity currents observed in laboratory studies, e.g., the evolution of the plume's head and its leading edge, and the development of Kelvin–Helmholtz instabilities. In a follow up study, Özgökmen et al. (2004) quantified the differences between 2D and three-dimensional (3D) simulations of bottom gravity currents. They found that the 3D results were in better agreement with laboratory experiments than the 2D counterpart. In particular, in the 2D experiments mixing due to entrainment was up to two times larger than in 3D. The authors attributed this discrepancy to the fact that 2D simulations cannot represent secondary instabilities that take place in 3D, resulting in a more rapid break down of the vortices. This difference was also observed in numerical simulations of gravity currents in the lock-exchange configuration (Härtel et al., 2000; Necker et al., 2002).

Özgökmen et al. (2006) used a combination of 2D and 3D numerical experiments to explore the effects of ambient stratification on the entrainment and properties of dense bottom currents that equilibrated at intermediate depths (i.e., forming interflows). Their simulations investigated the parameter space of  $0.125 \leq B_0 \leq 0.46$  and  $3^\circ \leq \theta \leq 7^\circ$ ; it will be shown later that these values of  $B_0$  are much larger than the range we find conducive to the development of flow splitting. Özgökmen et al. (2006) found that mixing by Kelvin–Helmholtz rolls did not penetrate all the way to the bottom of the density current and, therefore, the densest bottom water remained undiluted until the equilibration level was reached. They also demonstrated that entrainment and the proper-

ties of the product water depend only on the ambient stratification of the system, with no significant difference between 2D and 3D experiments. However, as noted by the authors, the regime where more vigorous mixing can occur remains to be investigated using a deeper domain, so that the mixing and consequent equilibration level with smaller  $B_0$  can be captured. Wobus et al. (2013) used a hydrostatic model to perform idealized three-dimensional simulations of a plume descending a conical slope into a rotating three-layer environment. By varying the inflow salinity and flow rate, they simulated flow regimes similar to those discussed above (interflow, underflow or split flow). Nonetheless, since their setup is based on a three layer system, it is not possible to classify their results in the context of  $B_0$ .

Based on the preceding review, we have identified the need for additional simulations to develop our understanding of whether flow splitting can occur in realistic oceanic outflows. Our new simulations cover the range of  $B_0$  for which we expect flow splitting, and use sufficiently high resolution ( $\Delta x = \Delta z = 5$  m) and non-hydrostatic dynamics needed to resolve shear-driven instabilities, an important mechanism for mixing in bottom gravity currents (Simpson, 1999). Inspired by the large range (5 to 20) of averaged turbulent Prandtl number values ( $Pr = \frac{\nu_h}{K_h} = \frac{\nu_v}{K_v}$ , where  $\nu_h/\nu_v$  and  $K_h/K_v$  are the turbulent horizontal/vertical viscosity and diffusivity, respectively) reported by Cortés et al. (2015), we investigate the sensitivity of the solutions to the following  $Pr$  values: 1, 10 and 50. Our simulations reveal, for the first time, that the flow splitting regime may occur in non-rotating linearly stratified oceanic environments. A conceptual model for the development of flow splitting is proposed based on a particular class of shear instability, namely those in the transition zone between Kelvin–Helmholtz and Holmboe instabilities, and on the development of an internal hydraulic jump. Finally, the conditions under which flow splitting might occur in oceanic outflows are discussed.

We emphasize that numerous simplifications, summarized in Section 4.4, in our simulations preclude confirming that split flows actually occur in oceanic outflows and make significant contributions to pathways for ventilation of dense shelf water into the deep ocean. However, these results identify a potentially important process that can be further investigated with more sophisticated numerical simulations and micro- and fine-structure measurement programs in candidate outflows.

## 2. Methods

### 2.1. Numerical model and dynamical configuration

The numerical simulations were conducted using the Massachusetts Institute of Technology general circulation model (MITgcm) (Marshall et al., 1997a; 1997b). The model was configured to solve the non-hydrostatic Boussinesq equations in the absence of rotation. MITgcm is a height-coordinate model that employs partial step topography (Adcroft et al., 1997) and the configuration employed in this study includes a free surface. Given the available computational resources, we only performed 2D simulations. Nevertheless, the 2D approximation is a good background for future 3D rotating studies. The relative inexpensiveness of 2D simulations allows for a more complete parameter space investigation, so that the controlling physical processes can be identified.

### 2.2. Experimental setup and parameters

The model domain is depicted in Fig. 2. It includes a 5 km wide flat continental shelf that is connected to a flat deep ocean (which is 50 km wide) through a constant shelf slope ( $\alpha$ ) of width  $L-5$  km, where  $L$  is the position where the slope intersects the ocean floor. The total length ( $L+50$  km) varies between 70 and 115 km,

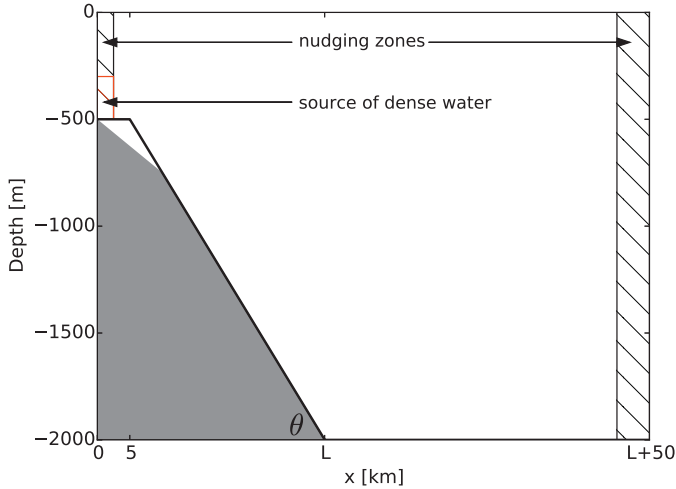


Fig. 2. Schematic of the model domain.

depending on the slope used. We performed a set of experiments *a priori* to ensure that the flow characteristics described here are not influenced by the total length of the domain. Three different shelf slopes were used: steep ( $\alpha = 0.1$ ), moderate ( $\alpha = 0.05$ ) and shallow ( $\alpha = 0.025$ ). This range covers the slopes of most continental shelves next to major oceanic outflows (Price and Baringer, 1994). The depth varies from 500 m at the shelf to 2000 m at the deep ocean. The geometry is consistent with the outer shelf and slope of the western Ross Sea, Antarctica (e.g., Padman et al. 2009), where shelf water depth is much larger than for most other global outflows. The dense water is prescribed in the first 2.5 km of the domain and below 300 m depth (red hatched region in Fig. 2). This configuration leads, in our simulations, to an initial outflow thickness  $h_0$  at the top of the slope (i.e.,  $x = 5$  km) of  $h_0 \sim 100$  m. This is a reasonable representation of the initial thickness observed in the major oceanic outflows (Legg et al., 2009; Price and Baringer, 1994).

To avoid complications that may arise through processes such as thermobaricity and cabelling (McDougall, 1987), we ignore salinity and use a linear equation of state as a function of temperature ( $T$ ) only:  $\rho(T) = \rho_0(1 - \alpha_T T)$ , where  $\rho_0 = 1025 \text{ kg m}^{-3}$  is the background density and  $\alpha_T = 5.3 \times 10^{-5} \text{ }^\circ\text{C}^{-1}$  is the thermal expansion coefficient. A passive tracer ( $\tau$ ) with an initial concentration of 1 was imposed within the dense plume to help visualize the flow behavior. No-slip boundary conditions are applied to the momentum equations at the bottom, while no-flux conditions are applied to tracers at the free surface. The side boundaries are kept closed and tracers and momentum are nudged towards the initial condition within regions that are 2.5 and 5.0 km wide on the left and right boundaries, respectively (see Fig. 2). A relaxation timescale of 360 seconds is used for both tracers and momentum. This procedure prevents internal waves being reflected at the boundaries and also provides a source and sink for momentum and tracers.

Both horizontal ( $\Delta x$ ) and vertical ( $\Delta z$ ) resolutions are set to 5 m, since previous 2D non-hydrostatic simulations of bottom gravity currents designed to study geophysical parameters and scales (with  $h_0 \sim 100$  m) have shown that such grid spacing is small enough to resolve shear instabilities such as Kelvin–Helmholtz billows (Özgökmen and Chassignet, 2002). These billows pull lighter water down under denser water, and the mixing associated with convective readjustment results in water with intermediate density. This is an important process that takes place at the interface between the dense water and the ambient lighter water. We avoid spurious mixing that takes place near steeper

topography of z-models by satisfying the condition  $\Delta x < \Delta z/\alpha$  (Winton et al., 1998). Hence, our simulations are able to capture the homogenization of tracers induced by the mixing driven by frictionally generated shear. To check for convergence of our solutions as functions of resolution, selected experiments were run at  $\Delta x = \Delta z = 2.5$  m and the results remained the same.

The initial ambient stratification ( $N$ ) is constant throughout the water column. Three different background density profiles are used:  $5.0 \times 10^{-4} \text{ s}^{-1}$  (weakly stratified);  $1.0 \times 10^{-3} \text{ s}^{-1}$  (moderately stratified); and  $2.5 \times 10^{-3} \text{ s}^{-1}$  (strongly stratified). In these cases, the density differences between the heaviest (i.e.,  $\rho$  at  $z = -2000$  m) and lightest (i.e.,  $\rho$  at  $z = 0$  m) water are 0.05, 0.2 and  $1.3 \text{ kg m}^{-3}$ , respectively. The initial density differences between the outflow and the ambient water just above it (i.e.,  $\rho$  at  $z = -300$  m) are set to  $\Delta\rho = 0.2 \text{ kg m}^{-3}$  in the weakly and moderately stratified cases, and to  $0.4 \text{ kg m}^{-3}$  in the strongly stratified cases. Therefore, in the absence of mixing, the imposed outflow densities would result in underflows for the weakly and moderately stratified cases and interflows for the strongly stratified experiments. Since the initial development of the system resembles lock exchange flows, the initial volume flux of the dense water per unit width can be computed as  $Q_0 \sim \sqrt{g'h_0}h_0$  (e.g., Özgökmen et al., 2004). With  $h_0 \sim 100$  m and using the values of  $N$  and  $\Delta\rho$  listed above, we vary  $B_0$  (as defined in Eq. (1)) by two orders of magnitude: 0.002, 0.016 and 0.13.

Laplacian friction was employed in the momentum equations. The vertical component of viscosity was set to  $\nu_v = 10^{-4} \text{ m}^2 \text{ s}^{-1}$ , while the horizontal component ( $\nu_h$ ) was  $7.5 \text{ m}^2 \text{ s}^{-1}$  in the strongly stratified cases, and  $5.0 \text{ m}^2 \text{ s}^{-1}$  otherwise. These values were chosen such that the grid Reynolds number ( $Re_g = U_{\max} \Delta x/\nu_h$ , where  $U_{\max}$  is the maximum plume velocity) was always less than 1.5. This condition is effective in eliminating grid-scale noise (Griffies et al., 2000; Ilicak et al., 2012), and is needed because momentum is advected using a second-order scheme that does not include an equivalent constraint. The horizontal viscosity values employed here are much larger than laboratory and realistic oceanic conditions, but they are required for numerical reasons. Our simulations are, therefore, at lower Reynolds number than laboratory and true oceanic flows.

Unlike momentum, tracers are advected using a third-order direct space-time flux limited scheme, which eliminates grid-scale noise by introducing numerical diffusivity where needed. Since the problem investigated here includes shocks and propagating fronts, the use of a flux limited scheme is essential to avoid unphysical behavior in terms of mixing (e.g., Ilicak et al., 2012; Marques and Özgökmen, 2014). Although this scheme does not require explicit tracer diffusivities, we set the horizontal ( $K_h$ ) and vertical ( $K_v$ ) diffusivities so that each experiment is run with the turbulent Prandtl number ( $Pr = \frac{\nu_h}{K_h} = \frac{\nu_v}{K_v}$ ) set to 1, 10 and 50. In stratified flows, momentum tends to diffuse faster than tracers, leading to  $Pr > 1$ . The reasoning behind varying  $Pr$  is to investigate how the flow behaves when the internal properties of the gravity current are changed. The values employed here are similar to the average  $Pr$  values (5 to 20) obtained in the numerical study of Cortés et al. (2015). Based on a set of experiments performed *a priori*, we verified that  $Pr = 50$  is the approximate maximum value that can be achieved in our experiments (i.e., when  $K_h$  is approximately equal to the implicit numerical diffusion). Ideally,  $Pr$  should be represented in terms of the gradient Richardson number ( $Ri(z) = \frac{N^2}{S^2}$ , where  $S = \frac{\partial u}{\partial z}$  is the vertical shear) using physically based formulations (e.g., Strang and Fernando, 2001; Elliott and Venayagamoorthy, 2011) However, none of these formulations has been implemented in the model employed here and, therefore, we choose to explicitly set the values of  $Pr$ .

**Table 1**  
Summary of parameters used in the numerical experiments.

Domain total length	70, 90 and 115 km
Grid resolution	$\Delta x = \Delta z = 5$ m
Maximum ocean depth	$H_{\max} = 2000$ m
Shelf depth	$H_{\text{shelf}} = 500$ m
Linear equation of state	$\rho(T) = 1025(1 - \alpha_T T)$
Thermal expansion coefficient	$\alpha_T = 5.3 \times 10^{-5} \text{ } ^\circ\text{C}^{-1}$
Shelf slope	$\alpha = 0.025, 0.05$ and $0.1$
Outflow thickness at $x = 5$ km	$h_0 \sim 100$ m
Ambient buoyancy frequency	$N = 5.0 \times 10^{-4}, 10^{-3}$ and $2.5 \times 10^{-3} \text{ s}^{-1}$
Initial $\rho_{\text{outflow}} - \rho_{\text{ambient}}$	$\Delta\rho = 0.2$ and $0.4 \text{ kg m}^{-3}$
Buoyancy number at $x = 5$ km	$B_0 = (2, 16$ and $130) \times 10^{-3}$
Vertical and horizontal viscosities	$\nu_v = 10^{-4} \text{ m}^2 \text{ s}^{-1}$ ; $\nu_h = 5$ and $7.5 \text{ m}^2 \text{ s}^{-1}$
Turbulent Prandtl number	$Pr = 1, 10$ and $50$
Time step	$\Delta t = 0.25$ s

Using the above mentioned values of  $B_0$ ,  $Pr$  and  $\alpha$ , a total of 27 2D numerical experiments were conducted. All simulations were started from rest and the model was stopped once it became possible to identify whether the flow has formed an interflow, underflow or split flow. In all experiments, the time step ( $\Delta t$ ) was set to 0.25 s. This value ensured that both the CFL condition and the stability parameter for the Laplacian friction were always satisfied. The model parameters are presented in Table 1.

### 3. Results

#### 3.1. Initial flow development

The initial flow development of the system is evaluated using snapshots of passive tracer ( $\tau$ ) concentration and density contours at different instants after each simulation was started. In the next two sections we focus on the nine experiments with  $\alpha = 0.1$  (steepest model slope). With this slope, we varied the initial buoyancy number,  $B_0 = 0.002$  (Fig. 3), 0.016 (Fig. 4) and 0.13 (Fig. 5); and the turbulent Prandtl number,  $Pr = 1, 10$  and  $50$  (on each figure: left, center and right panels, respectively).

The initial development of the system is similar to that of the so-called lock-exchange flow (e.g., Simpson, 1999), in which the denser fluid propagates downslope while the lighter fluid flows in the opposite direction along the top boundary of the domain. All cases show the development of a characteristic head as the leading edge of the outflow propagates downslope (panels a-c on each of Figs. 3 to 5). The initial growth of the head was observed in all experiments, as less dense ambient water was entrained into the leading edge of the plume. As  $Pr$  increases (i.e., when the diffusivities are reduced), the plume becomes less diluted and the vertical gradient of  $\tau$  at the tail of the current (i.e., the region behind the head) becomes sharper (panels a-c on each of Fig. 3 to 5).

Once the head of the current has passed  $x \sim 15$  km, density interfaces at the tail of the current begin to roll up (panels d-f on each of Fig. 3 to 5). These counter-clockwise vortices are indicative of shear instability, in which unstable waves entrain less dense fluid into the dense current. Both the horizontal and vertical dimensions of these features vary between 50 and 200 m and, therefore, are resolved by the grid resolution employed here ( $\Delta x = \Delta z = 5$  m). There is a general tendency for these vortices to coalesce and form larger structures via pairing, which is a well-documented behavior of 2D shear instabilities (e.g., Özgökmen and Chassignet, 2002). These vortices would be significantly smaller if the effects of three-dimensionality were included in the simulations (Härtel et al., 2000; Özgökmen et al., 2004), potentially affecting the mixing of the flow. At this point, the initial development of clockwise vortices due to frictionally generated shear is also evident in the bottom boundary layer (red region in the inset of panels d-f on each of Fig. 3 to 5; see also correspondent animations in the Auxiliary Material). These features act as sinks of

kinetic energy and, unlike the upper shear instability at the interface, tend to homogenize the water properties next to the bottom (i.e., they have less effect on mixing of tracers). Further analyses of the different types of shear instabilities taking place in these simulations are presented in Section 3.4.

#### 3.2. Flow regimes

In the simulations where  $B_0 = 0.002$  (Fig. 3), the initial head remains attached to the bottom current until it reaches the deep ocean (Fig. 3 d to f). Snapshots taken at the end of the simulations clearly show the generation of an underflow, regardless of the value of  $Pr$  (Fig. 3 g to i). The only differences are that the plume becomes less diluted and the size of the instabilities gets smaller as  $Pr$  increases. When  $B_0 = 0.016$  (Fig. 4), the head merges with the trailing current before the leading edge reaches the end of the slope (Fig. 4 d to f). Soon after, the behavior of the current differs among the simulations. For  $Pr = 1$ , the entire plume detaches from the bottom forming an interflow (Fig. 4g). However, when  $Pr = 10$  or  $50$ , a portion of the upper part of the current detaches from the slope and flows out into the interior, while the lower part of the current remains flowing towards the bottom of the domain (Fig. 4 h and i, respectively). In both cases, a clear discontinuity (or shock) separating two different mixing regions occurs around  $x \sim 18$  km. The onshore region is characterized by a “pool” of homogeneous fluid (light blue shading in Fig. 4h and i) sitting on the top of the bottom current. This fluid has been strongly diluted by shear instabilities and subsequent mixing. The offshore region is characterized by thickening of the plume, with water classes ranging between the less dense intermediate plume to the denser and less diluted plume next to the bottom. This sudden increase in the plume thickness suggests the development of an internal hydraulic jump, and we explore this further in Section 3.4.2. From Fig. 4 h and i, it is also evident that, as  $Pr$  increases, the lower part of the current is less diluted and, therefore, it penetrates to a greater depth (e.g., the distance between the upper and lower plumes increases). Nonetheless, in both cases the structure of the system resembles the flow splitting regime observed by Baines (2008) (see Fig. 1).

Finally, when  $B_0 = 0.13$  (Fig. 5), for all values of  $Pr$  the head of the plume detaches from the bottom before the outflow reaches the end of the slope (Fig. 5 d to f). This plume then propagates towards the interior, resulting in an interflow (Fig. 5 g to i). As in the cases described above, as  $Pr$  increases, the gravity current gets less diluted and the spatial scale of features become smaller. There is a clear distinction between the lower and upper part of the flow when  $Pr \geq 10$ , where the fluid is significantly more diluted in the latter (Fig. 5 h and i). This distinction becomes more pronounced as  $Pr$  increases. However, since  $N$  in these experiments is relatively large, this condition is not enough to result in flow splitting.

#### 3.3. Sensitivity to shelf slope

Laboratory experiments by Baines (2001); 2005) show that the bottom slope plays a key role in determining the flow regime of downslope flows into stratified environments. Therefore, it is useful to verify if the same reasoning applies to the parameter space employed in our simulations. To this end, we present additional simulations using  $\alpha = 0.05$  and  $0.025$ . The remaining parameters in these runs, namely  $B_0$  and  $Pr$ , are identical to those described in Section 3.1. Hence, a total of eighteen additional experiments are described here. From snapshots of  $\tau$  taken at the end of these simulations, a qualitative description of the different flow regimes is presented below.

As in the steep slope cases, when  $B_0 = 0.002$  and  $\alpha = 0.05$  (Fig. 6 a to c) or  $\alpha = 0.025$  (Fig. 7 a and c), the underflow regime is generated regardless of  $Pr$ . Again, the only differences between

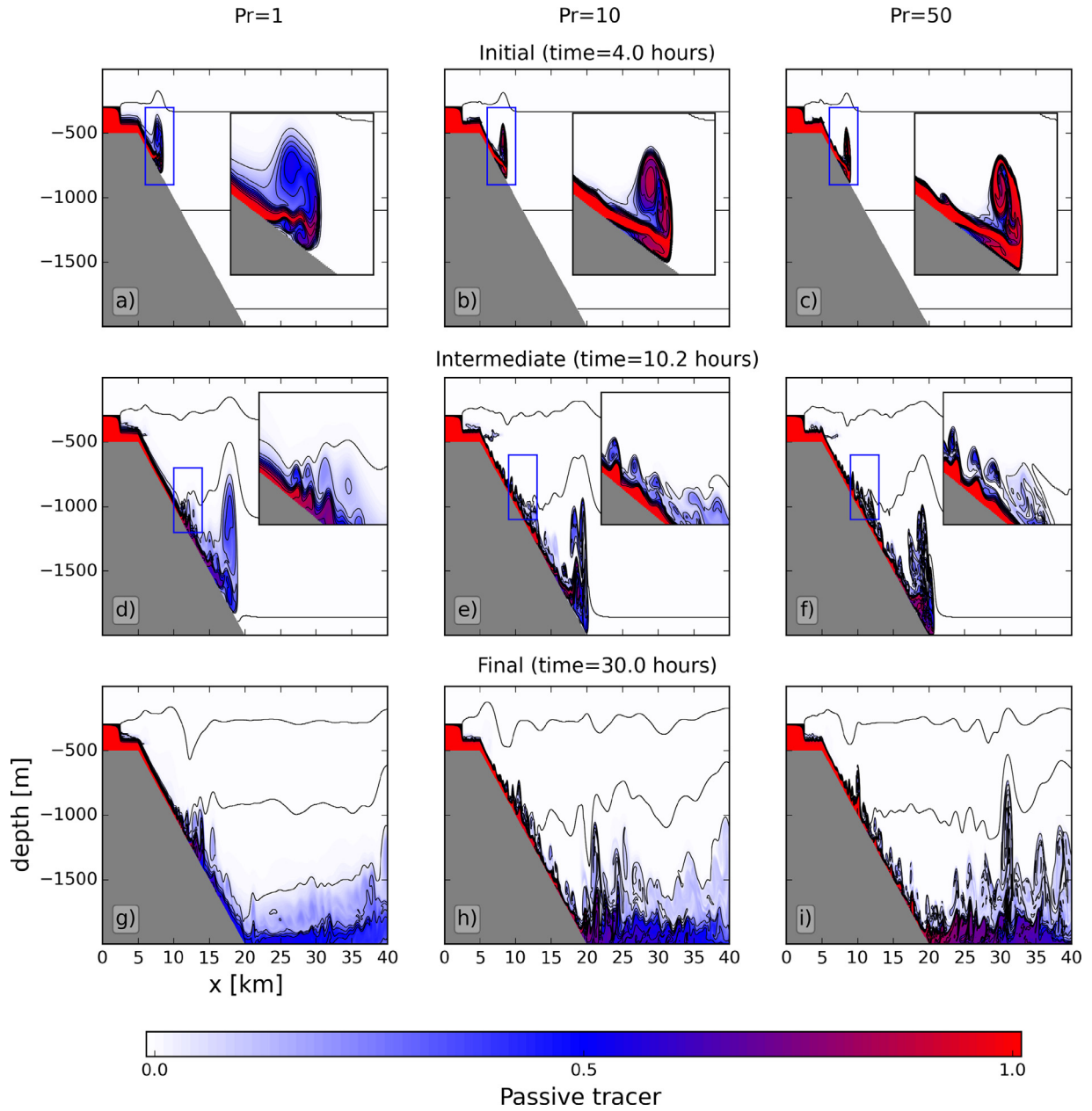


**Fig. 3.** Time evolution of passive tracer distribution ( $\tau$ , color) and density contours ( $\text{kg m}^{-3}$ , black lines plotted every  $0.02 \text{ kg m}^{-3}$ ) for experiments with  $\alpha = 0.1$ ,  $B_0 = 0.002$  and  $Pr = 1, 10$  and  $50$  (left, center and right panels, respectively). The initial evolution of the plume's head are shown at the top panels, intermediates states are shown in the middle panels and the conditions at the end of the simulations are shown in the bottom panels. The underflow regime is always generated, regardless of  $Pr$ . The blue boxes in the top and middle panels denote the boundaries for the closeups shown in the plots. Only a portion of the computational domain is displayed. Corresponding animations are available in the auxiliary materials (ms01, ms02 and ms03 refer to experiments with  $Pr = 1, 10$  and  $50$ , respectively). (For interpretation of the references to colour in this figure legend, the reader is referred to the web version of this article.)

these cases is that the plume gets less diluted and smaller length-scale features become apparent as  $Pr$  increases.

When  $B_0 = 0.016$ ,  $Pr = 1$  and  $\alpha = 0.05$  (Fig. 6d) or  $\alpha = 0.025$  (Fig. 7d), the current detaches from the bottom and forms an interflow. For  $Pr \geq 10$ , flow splitting also occurs under a moderate slope  $\alpha = 0.05$  (Fig. 6 e and f) and under a shallow slope  $\alpha = 0.025$  (Fig. 7 e and f). In comparison to the steep slope cases (Fig. 4h and i), as the slope decreases the plume needs to travel further to result in flow splitting. A thin “tongue” of intermediate density appears between the upper and lower parts of the plume (Fig. 6e). This feature is not present when  $\alpha = 0.1$ .

Finally, when  $B_0 = 0.13$ , all simulations lead to the interflow regime, regardless of  $\alpha$  and  $Pr$ .

In summary, for given  $B_0$  and  $Pr$  values, the flow regimes obtained using intermediate ( $\alpha = 0.05$ ) and shallow ( $\alpha = 0.025$ ) slopes are identical to those obtained using a steep slope ( $\alpha = 0.1$ ). In the following sections, we focus on simulations conducted with the steep slope ( $\alpha = 0.1$ ) since less disk space was required to save high frequency output, used in the following analysis, during the initial development of the flow in these runs.

### 3.4. Internal properties of the outflow

#### 3.4.1. Buoyancy and velocity profiles

We now examine how buoyancy and cross-slope velocity profiles vary among our simulations. We define buoyancy as  $\bar{b}(z) = -g(\bar{\rho}(z) - \rho_0)/\rho_0$ , and cross-slope velocity,  $\bar{u}(z)$ , profiles, with

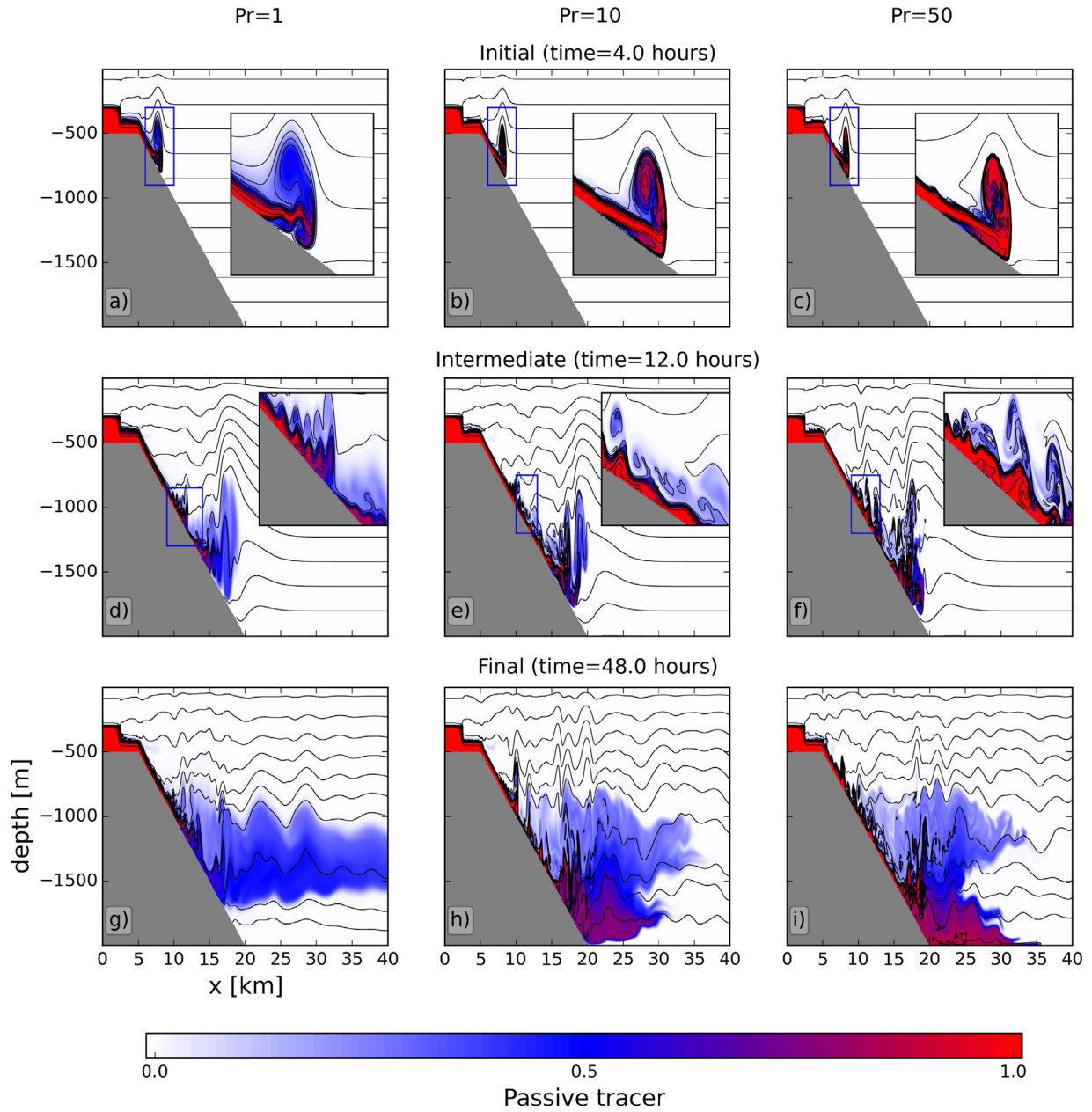


**Fig. 4.** Same as Fig. 3, but for  $B_0 = 0.016$ . The interflow regime occurs when  $Pr = 1$  (left column), while flow splitting occurs when  $Pr \geq 10$  (middle and right columns). Corresponding animations are available in the auxiliary materials (ms04, ms05 and ms06 refer to experiments with  $Pr = 1, 10$  and  $50$ , respectively).

over-lines indicating averages over space and time. These profiles were computed by first extracting  $\rho(z, x, t)$  and  $u(z, x, t)$  for  $5.5 \leq x \leq 6.0$  km (top of slope) then spatially averaging the data based on the distance of each level with respect to the bottom. Next, the data were averaged over time for  $15 \text{ h} \leq t \leq 20 \text{ h}$  with an output period of 120 seconds. Since shear instabilities become more pronounced at later times and downstream of this region, this procedure provides a robust representation of the profiles, with relatively small standard deviations from the mean values.

As  $Pr$  increases, the buoyancy gradient ( $\partial \bar{b} / \partial z$ ) becomes sharper while the shear ( $\partial \bar{u} / \partial z$ ) does not change significantly throughout most parts of the water column (Fig. 8). When  $Pr = 1$ , the upper part of the profile (height  $\sim 80$  m above bottom) displays a smoother shape than the corresponding profiles with  $Pr = 10$  and  $50$ . For a fixed  $Pr$  value, both  $\bar{u}(z)$  and  $\bar{b}(z)$  are overall very similar among the experiments. The only difference is that  $\Delta \bar{u}$  and  $\Delta \bar{b}$  (defined in Fig. 9) are slightly larger in cases where  $B_0 = 0.13$ .

To quantify the differences among profiles, the following idealized curves for  $\bar{u}(z)$  and  $\bar{b}(z)$ , respectively, are fitted to the model data using the non-linear least squares algorithm available in the open source Python library SciPy:<sup>2</sup>

$$\tilde{u} = -\frac{\Delta u}{2} \tanh\left(\frac{2}{h_u} z\right); \quad (4)$$

$$\tilde{b} = \frac{\Delta b}{2} \tanh\left(\frac{2}{h_b} z\right), \quad (5)$$

where  $h_u$  is the thickness of the shear layer,  $z$  is the vertical coordinate centered at the level of maximum shear,  $\Delta u$  and  $\Delta b$  are the velocity and buoyancy differences, respectively (see Fig. 9). Profiles fitted to the model data using Eqs. (4) and (5) are also shown in

<sup>2</sup> [http://docs.scipy.org/doc/scipy-0.16.1/reference/generated/scipy.optimize.curve\\_fit.html](http://docs.scipy.org/doc/scipy-0.16.1/reference/generated/scipy.optimize.curve_fit.html)

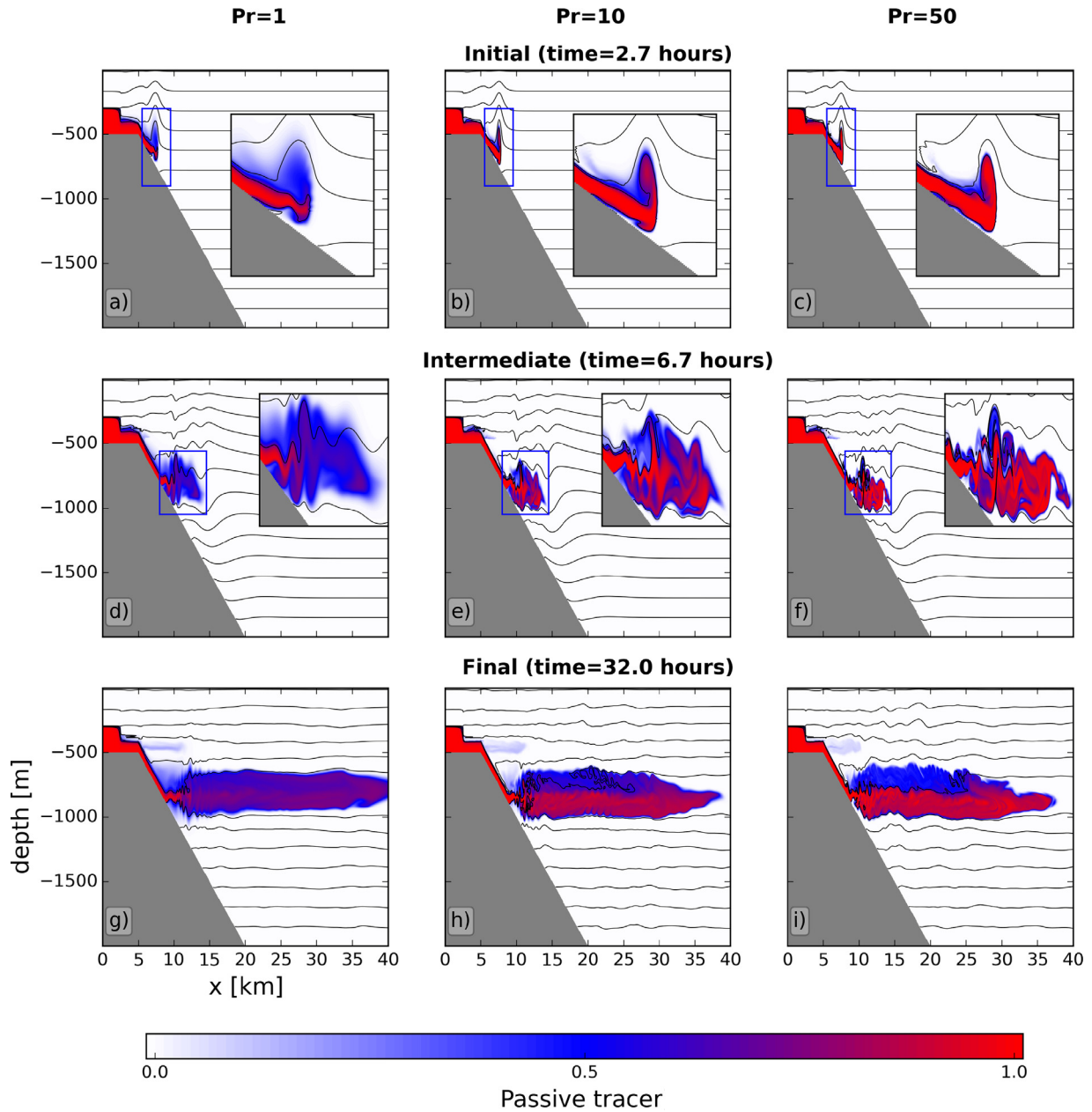


**Fig. 5.** Same as Fig. 3, but for  $B_0 = 0.13$ . The interflow regime is always generated, regardless of  $Pr$ . Density contours (black lines) are plotted every  $0.1 \text{ kg m}^{-3}$ . Corresponding animations are available in the auxiliary materials (ms07, ms08 and ms09 refer to experiments with  $Pr = 1, 10$  and  $50$ , respectively).

Fig. 8 (black and red stars, respectively). The idealized curves are not meant to capture boundary layer shears (which is of less importance here) but to represent the environment in which interfacial instabilities develop. A few important dimensionless parameters for the evolution of the flow can now be defined: the scale ratio,  $R = h_u/h_b$ , where  $h_b$  is thickness of the stratified layer (see Fig. 9); the bulk Richardson number,  $J = \Delta b h_u / \Delta u^2$ ; and the central Richardson number,  $Ri_0 = JR$ . The central Richardson number quantifies the relative importance of stratification and shear and it is equivalent to the gradient Richardson number,  $Ri(z) = \frac{\partial b / \partial z}{(\partial u / \partial z)^2}$  evaluated at the center of the shear layer. An additional parameter that is usually considered in studies of stratified shear flows (e.g., Smyth et al., 2007) is the asymmetry factor ( $a$ ), which quantifies the offset between the centers of the shear and stratified layers. However, we neglect this parameter since the offset in all profiles

investigated here is very small (maximum of  $\pm 5 \text{ m}$ , or one model grid cell).

For all profiles shown in Fig. 8,  $R$  increases as  $Pr$  increases (Fig. 10a). The most significant change occurs when  $Pr$  varies between 1 and 10, where  $R$  approximately doubles (i.e.,  $h_u \sim 2 \times h_b$ ). As  $Pr$  changes from 10 to 50, the corresponding increase in  $R$  is relatively small ( $\sim 20\%$ ) and at this point  $h_b$  is approaching the smallest value that we can resolve ( $\sim 15 \text{ m}$ , or  $3 \times \Delta z$ ) given the vertical resolution employed here ( $\Delta z = 5 \text{ m}$ ). The thickness of the shear layer ( $h_u$ ) decreases as  $Pr$  increases (Fig. 10b), while  $Ri_0$  gets larger as  $Pr$  increases (Fig. 10b). Again, the most significant changes in  $h_u$  and  $Ri_0$  occur in the  $Pr = 1$  to  $Pr = 10$  transition. In the absence of instabilities and given a time scale  $\lambda$ , both thicknesses will grow by diffusion according to  $h_u \sim (\nu_v \lambda)^{1/2}$  and  $h_b \sim (K_v \lambda)^{1/2}$ . However, after 20 hours and given the small values of  $\nu_v$  and  $K_v$  employed here (see Table 1),  $h_u$  and  $h_b$  cannot grow to the

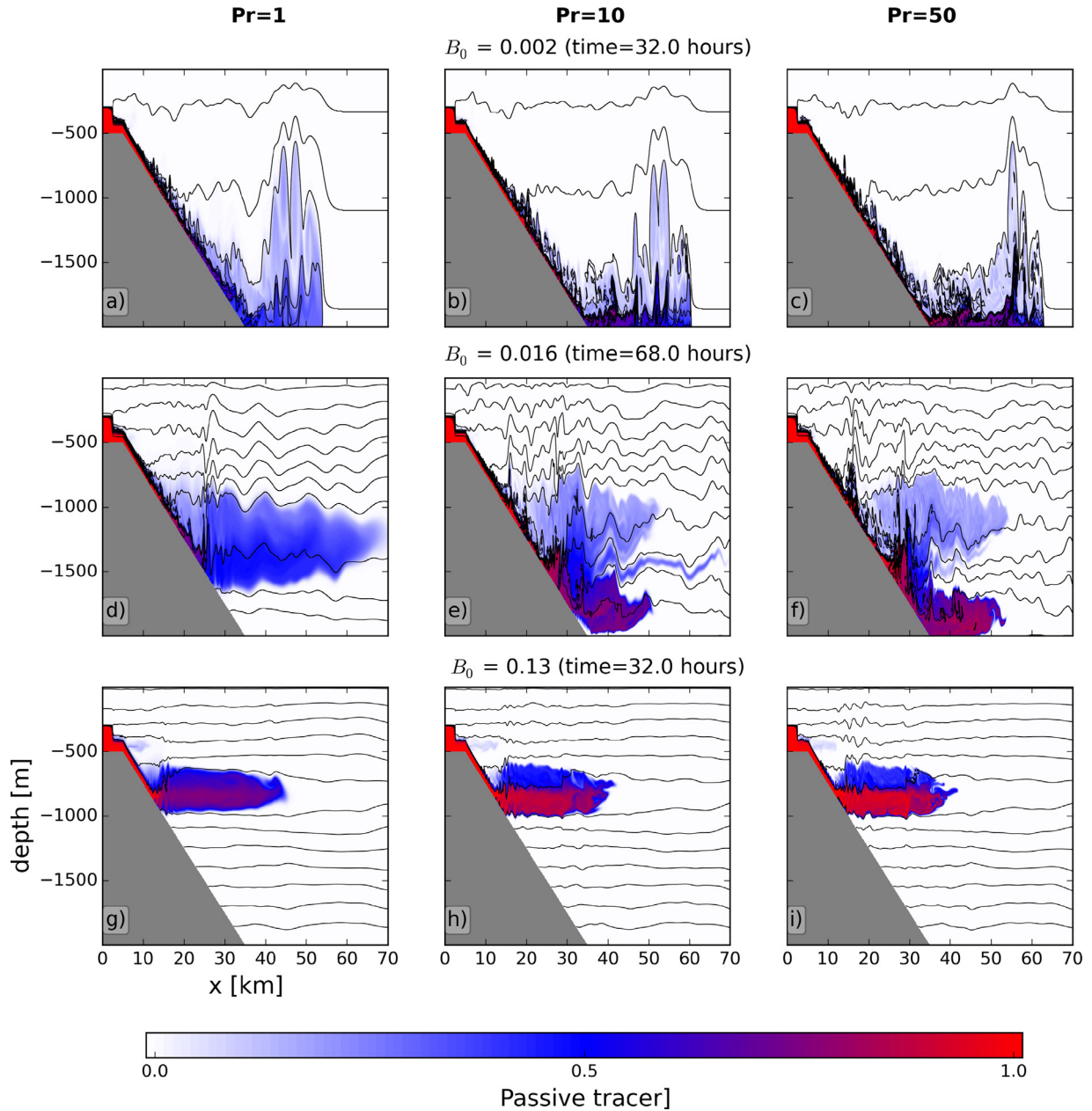


**Fig. 6.** Snapshots of passive tracer distribution ( $\tau$ , color) and density contours ( $\text{kg m}^{-3}$ , black lines) taken at the end of the simulations for experiments with  $\alpha = 0.05$ . Flow splitting occurs when  $B_0 = 0.016$  and  $Pr \geq 10$  (panels e and f). The following parameters are varied: (from left to right)  $Pr = 1, 10$  and  $50$ ; (from top to bottom)  $B_0 = 0.002, 0.016$  and  $0.13$ . Density contours are plotted every  $0.02 \text{ kg m}^{-3}$  in the top and middle panels, and every  $0.1 \text{ kg m}^{-3}$  in the bottom panels.

observed values just because of diffusion. Although instabilities in the upper part of the slope were not pronounced during the period when the profiles were averaged (between 15 and 20 hours), we speculate that  $h_u$  and  $h_b$  develop due to the horizontal advection of buoyancy and momentum in a sloped bottom. This is a consequence of the vertical coordinate employed here and the results might differ under different vertical coordinates, such as terrain-following or isopycnals.

The necessary condition for the development of instabilities based on the Miles-Howard criterion (Howard, 1961; Miles, 1961), namely  $Ri(z) < 0.25$ , is satisfied in all cases (Fig. 10c); recall that  $Ri_0$  is equivalent to  $Ri(z)$  evaluated at the center of the shear layer. Although this condition is not sufficient for the development of instabilities, the results presented in the previous sections clearly show that instabilities occur in all simulations. It is not clear, however, whether these instabilities are all of the same type. There is a

continuous spectrum of modes that range from Kelvin-Helmholtz to Holmboe instabilities and beyond, and it is not trivial to identify them (this is also beyond the scope of this paper). However, the fact that  $R$  changes significantly as  $Pr$  increases from 1 to 10 suggests that different instabilities might be occurring (see, e.g., Smyth and Winters, 2003; Hogg and Ivey, 2003) and we will discuss this further in Section 4.1.

### 3.4.2. Internal hydraulic jump

The presence of internal hydraulic jumps is often associated with discontinuities in the density and velocity fields, where the flow transitions from supercritical to subcritical conditions (e.g., Holland et al., 2002; Legg and Klymak, 2008; Long, 1953, 1954). Supercritical flows are characterized by  $Fr \geq 1$ , i.e., the mean bottom current speed  $U$  exceeds the long-wave phase speed  $c_p = \sqrt{g'h}$ , while the flow is subcritical when  $Fr < 1$ . It is there-

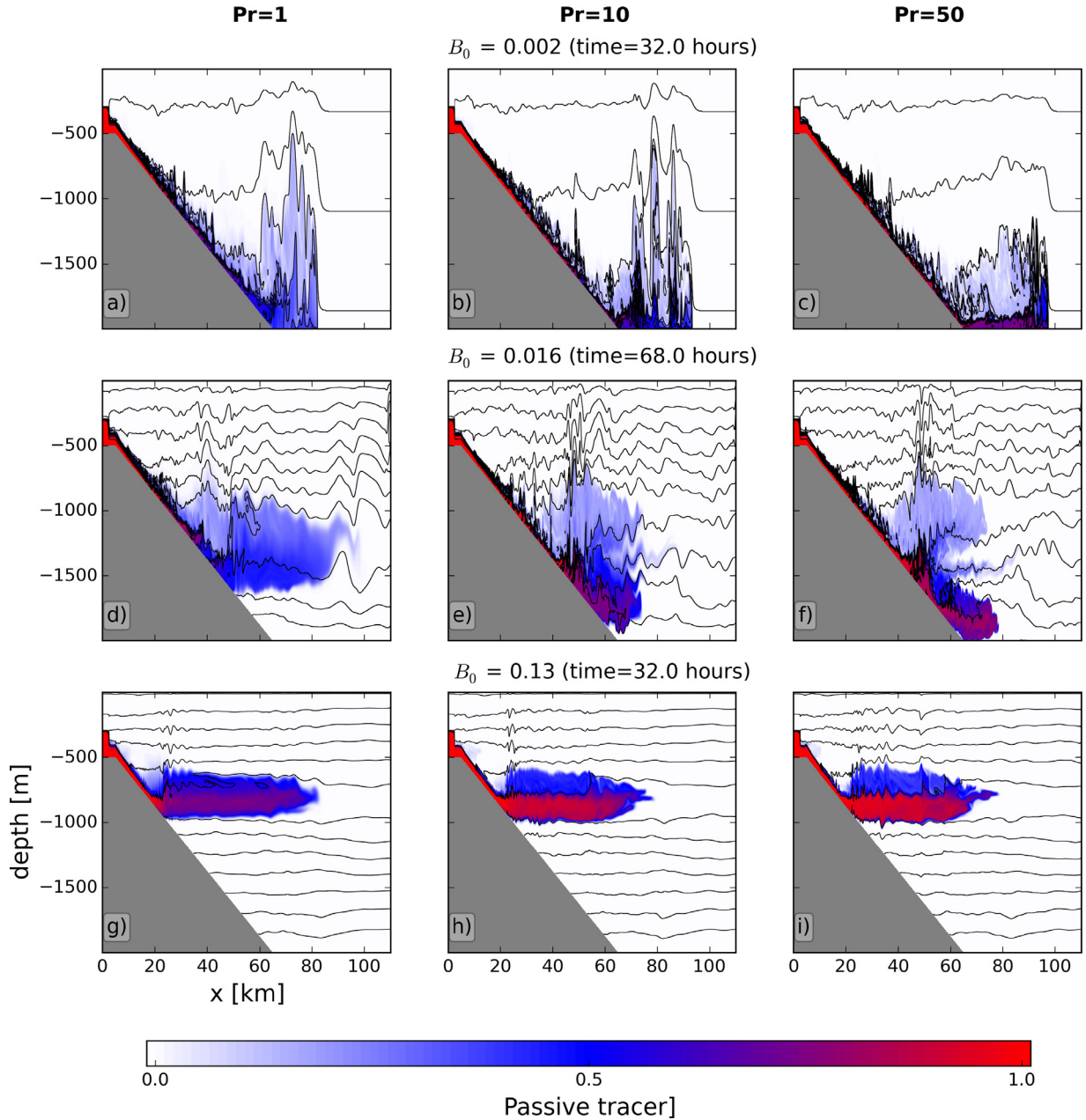


Fig. 7. Same as Fig. 6, but for experiments with  $\alpha = 0.025$ . Flow splitting occurs when  $B_0 = 0.016$  and  $Pr \geq 10$  (panels e and f).

fore of interest to investigate whether and why internal hydraulic jumps occur in the different flow regimes simulated here. Following Wobus et al. (2013), the thickness of the plume,  $h(x, t)$ , is defined as the height above the bottom where the passive tracer concentration  $\tau$  drops below 50% of its value at the seabed. This selection is somewhat arbitrary and  $h(x, t)$  is sensitive to the chosen threshold value. Nonetheless, the outcomes shown below are still valid when the upper threshold of  $\tau$  was varied within 35% to 65% of the bottom value. In the following analysis, we focus on experiments where  $\alpha = 0.1$  and  $Pr = 50$  since the internal hydraulic jump is more pronounced under these conditions. Just the region within the shelf slope is evaluated and the values are averaged in time over the last 10 hours of each simulation (denoted by angle brackets,  $\langle \rangle$ ).

When an underflow is generated ( $B_0 = 0.002$ ),  $\langle h \rangle$  is almost constant throughout the slope (Fig. 11a). Similarly, when the plume results in an interflow ( $B_0 = 0.13$ ),  $\langle h \rangle$  remains constant until the

current detaches from the slope (Fig. 11a). However, when flow splitting occurs ( $B_0 = 0.016$ ), there is a strong discontinuity in  $\langle h \rangle$  at  $x \sim 16$  km (Fig. 11a). Indeed, the time-averaged Froude numbers,  $\langle Fr \rangle$ , in the flow splitting regime show a transition from supercritical to subcritical, consistent with the discontinuity in  $\langle h \rangle$  (Fig. 11b). In contrast,  $\langle Fr \rangle$  remains supercritical in the interflow and underflow regimes (Fig. 11b; noticed that the purple line drops off to zero as the plume detaches from the slope, as shown in Fig. 11a).

To further investigate what is causing the internal hydraulic jump in the flow splitting regime, we compute the density excess of the system as follows:

$$\rho^*(x, z, t) = \rho(x, z, t) - \rho(x, z, t = 0), \quad (6)$$

where  $\rho(x, z, t = 0)$  is the initial density field. Time-averaged density excess ( $\rho^*$ ) for a simulation that results in flow splitting ( $B_0 = 0.016$ ) clearly shows a wide region with densities smaller than

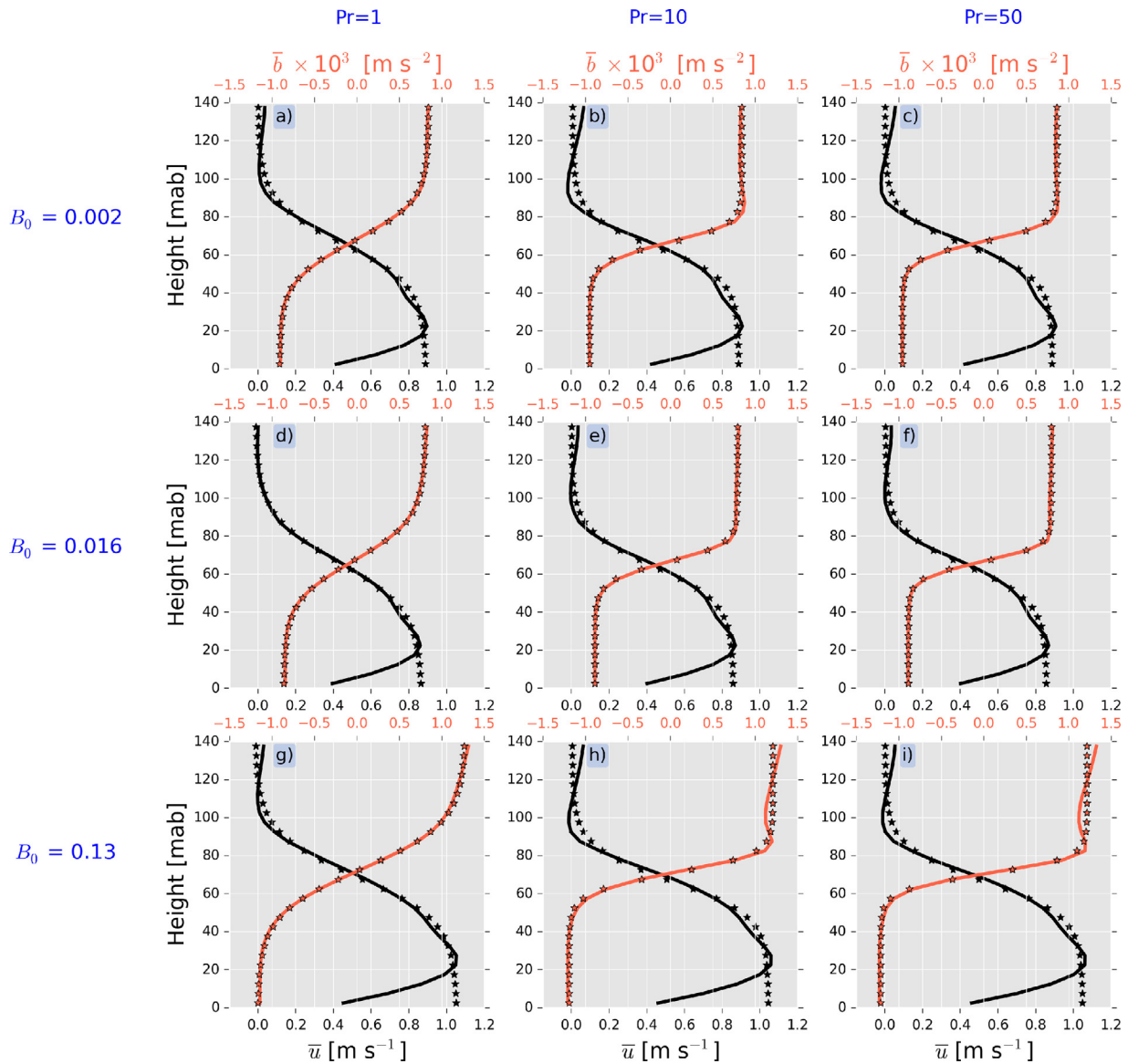


**Fig. 8.** Vertical profiles of cross-slope velocity ( $\bar{u}$ , black lines) and buoyancy ( $\bar{b}$ , red lines) for simulations with  $B_0 = 0.002, 0.016$  and  $0.13$  (from top to bottom, respectively), and  $Pr = 1, 10$  and  $50$  (from left to right, respectively). These plots highlight how the vertical gradient in buoyancy ( $\partial\bar{b}/\partial z$ ) increases (i.e., the buoyancy profile gets sharper) as  $Pr$  increases. Height is shown as meters above bottom (mab). Over-lines indicate averages over space and time, see text for further details. Black and red stars represent the profiles fitted using Eqs. (4) and (5), respectively. (For interpretation of the references to colour in this figure legend, the reader is referred to the web version of this article.)

those at the start of the run (Fig. 12). This region coincides with the pool of homogeneous  $\tau$  described earlier and shown in Fig. 4i. One possible explanation for the formation of this buoyant region, where  $\langle\rho^*\rangle$  is negative, is the development of Holmboe-like instabilities upstream of this region. These instabilities engulf parcels from the upper part of the gravity current leading to detrainment. The detrained parcels of fluid are initially advected downstream due to inertia, leading to further mixing with ambient water (i.e., entrainment). The result is that the detrained water parcels are brought to depths greater than those where they would be neutrally buoyant.

This previous description is supported by the time evolution of 1444 particles advected offline using a fourth-order Runge–Kutta scheme (Fig. 13). The particles were initially seeded between  $14 \text{ km} \leq x \leq 20 \text{ km}$  and  $-2000 \text{ m} \leq z \leq -800 \text{ m}$ , every  $150 \text{ m}$  in the horizontal direction and  $25 \text{ m}$  in the vertical direction (Fig. 13a, see also corresponding animation available in the auxiliary materials). The velocity field was updated every 120 sec-

onds and the particles were advected between  $15 \text{ h} \leq t \leq 45 \text{ h}$ . The movement of particles reveals a slow counter-clockwise circulation on the top of the density current, between approximately  $10 \text{ km} \leq x \leq 18 \text{ km}$ . This is also the region where  $\langle\rho^*\rangle$  is negative (Fig. 12), which reinforces the previous explanation that detrained parcels of fluid are advected downstream of their level of neutral buoyancy, and then rise due to buoyancy.

## 4. Discussion

### 4.1. Conceptual model for flow splitting in linearly stratified environments

Previous sections have elucidated the different flow regimes that may occur in numerical simulations of oceanic dense-water outflows with linearly stratified environments. However, a conceptual model for the development of the flow splitting regime under such conditions is still missing. This model is now presented, fol-

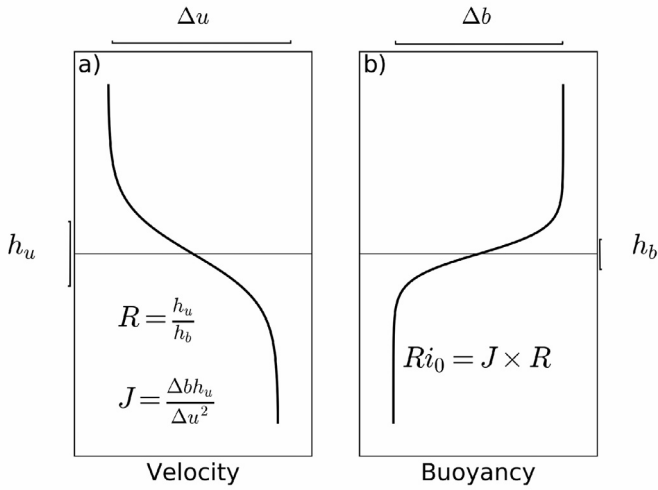


**Fig. 9.** Schematic representation of (a) velocity and (b) buoyancy profiles constructed using Eqs. (4) and (5), respectively. Also shown are the important dimensionless parameters,  $R$  and  $Ri_0$ , used to characterize the evolution of the flow (see text for their definition).

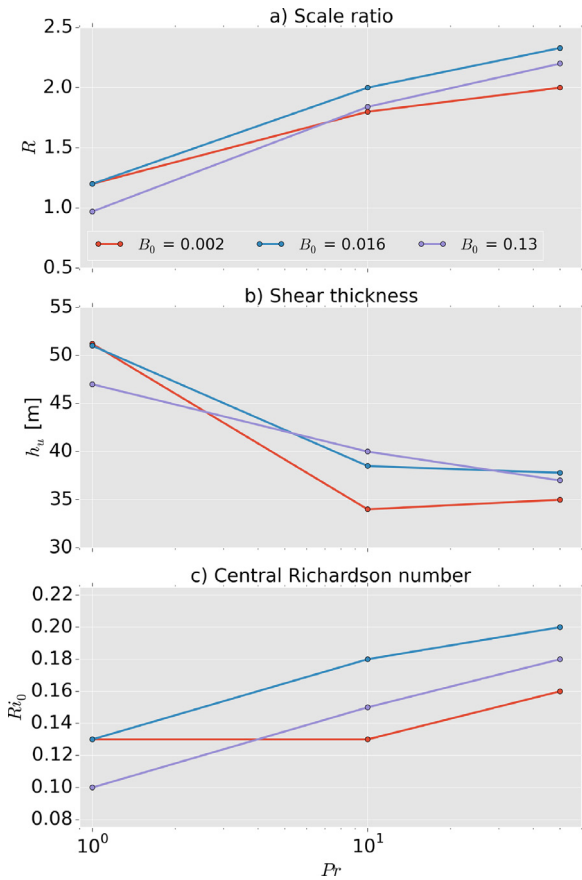


**Fig. 10.** Prandtl number versus (a) scale ratio,  $R$ ; (b) shear thickness,  $h_u$  [m]; and (c) central Richardson number,  $Ri_0$ . Results from simulations with different  $B_0$  values are shown.

lowed by a discussion on how it compares with processes previously suggested in the literature. The description that follows applies to all experiments where  $B_0 = 0.016$  and  $Pr \geq 10$ , regardless of  $\alpha$ .

A summary of the processes occurring in the flow splitting regime is depicted in Fig. 14. The outflow is initially supercritical ( $Fr > 1$ ), with shear-generated instabilities developing at the top

boundary of the current (dark blue circles in Fig. 14). Additional shear-induced instabilities also occur in the bottom boundary layer (yellow circles in Fig. 14), but these act as sinks of kinetic energy and just homogenize the dense plume, i.e., they have less effect on mixing than the instabilities in the upper interface. The upper instabilities are characterized by buoyancy interfaces that are thinner than the shear interfaces (i.e.,  $R > 2$ ), which is suggestive of Holmboe-like instabilities (e.g., Smyth and Winters, 2003; Hogg and Ivey, 2003). They lead to detrainment of small blobs of fluid that are then advected downstream, as a consequence of inertia, to form a “pool” of stagnant buoyant fluid sitting on the top of the main current (Fig. 13; also highlighted by the light blue region in Fig. 14). This buoyant water is brought to depths below its level of neutral buoyancy relative to the environment (Fig. 12). Since there is a constant injection of detrained fluid upstream, the presence of a region of buoyant fluid results in a slow counter-clockwise circulation on the top of the density current (Fig. 13; also highlighted in Fig. 14). A small fraction of fluid then propagates towards the deep ocean away from the slope, forming the intermediate plume as the fluid becomes neutrally buoyant, while the rest of the fluid recirculates back towards the upper part of the slope. As the main density current propagates underneath the region of stagnant fluid, it gets thicker but its velocity is approximately constant. Both interfacial and near-bottom shear instabilities also occur at this state. The flow then transitions from a supercritical condition ( $Fr > 1$ ) to a slower and more uniform subcritical condition ( $Fr < 1$ ). This transition results in an internal hydraulic jump, where kinetic energy is converted into potential energy as a consequence of strong mixing (red region in Fig. 14). Additional water masses are then generated, filling the gap between the upper and lower plumes. The fluid in the bottom boundary layer undergoes little mixing with ambient water, so that the lower abyssal plume is almost undiluted.

There are many similarities between the mechanism described above and the scenario described by Baines (2008) based on laboratory experiments. Baines (2008) suggested that detrainment in the upper part of the current could lead to the development of the intermediate plume observed in Fig. 1. Detrainment has been previously described as a consequence of Holmboe-like instabilities generated due to the mutual interaction between a gravity wave on the interface and a vorticity wave traveling above the density current (Baines, 2001). As discussed above, detrainment of small blobs of fluid in combination with the characteristics of the internal properties of the flow also suggest the presence of Holmboe-like instabilities in our simulations. However, unlike previous studies (e.g., Baines, 2001), the offset between the interfacial wave and the line of maximum vorticity is insignificant in our simulations (maximum of 5 m or one grid cell). Rather, the instabilities in our simulations are triggered as a consequence of the buoyancy interface being sharper than the shear interface (i.e.,  $R > 2$ ). Consistent with our numerical results, estimates of the Richardson number in the two laboratory experiments that resulted in flow splitting were more than two times larger than those experiments where splitting did not occur (see Table 1 in Baines (2005)). Based on a “conspicuous upward bubbling” (Fig. 1), Baines (2008) suggested that the fluid supplying the intermediate plume arose from the vicinity of the bottom plume. This indicates that portions of the plume were advected to depths greater than those where they would be neutrally buoyant and, therefore, the fluid rose due to buoyancy. This is also consistent with our simulations where flow splitting occurs.

The internal hydraulic jump is the only important feature observed in our simulations that was not mentioned by Baines (2008). It is possible, however, that the measurements performed in the laboratory experiments were not adequate to detect this phenomenon. Such jumps are common features of oceanic outflows (e.g., Pratt et al., 2007; Legg et al., 2009), but their pres-

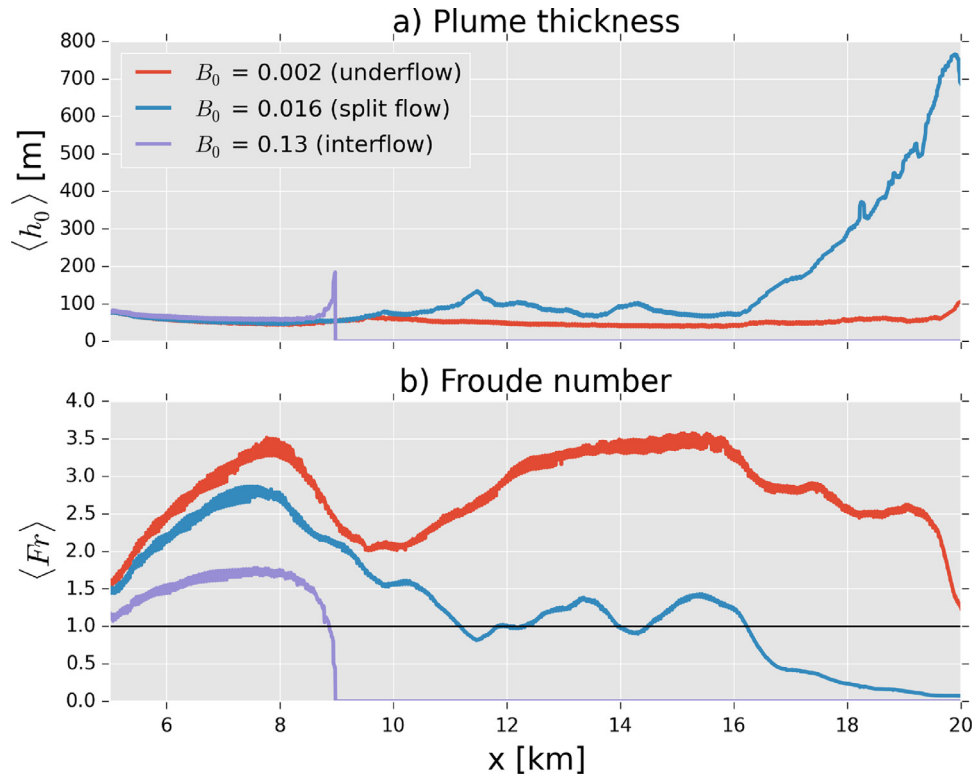


**Fig. 11.** Time-averaged plume thickness,  $\langle h_0 \rangle$  (a) and Froude number,  $\langle Fr \rangle$  (b) as a function of cross-slope distance for selected experiments where  $\alpha = 0.1$ ,  $Pr = 50$  and  $B_0 = 0.002$  (underflow), 0.016 (split flow) and 0.13 (interflow).

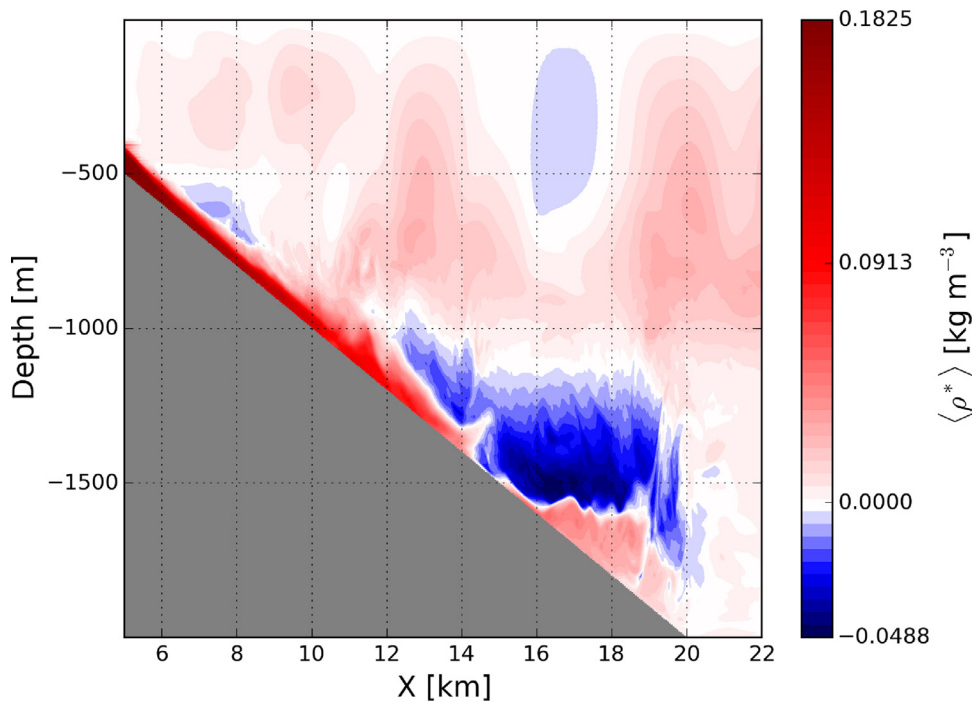


**Fig. 12.** Time-averaged density excess ( $\rho^*$ ) as a function of depth and cross-slope distance for an experiment where flow splitting occurs ( $\alpha = 0.1$ ,  $Pr = 50$  and  $B_0 = 0.016$ ). Blue contours show regions where water is less dense than the initial ambient water at the same depth; i.e., it indicates where water parcels are brought to depths greater than those where they would become neutrally buoyant. (For interpretation of the references to colour in this figure legend, the reader is referred to the web version of this article.)

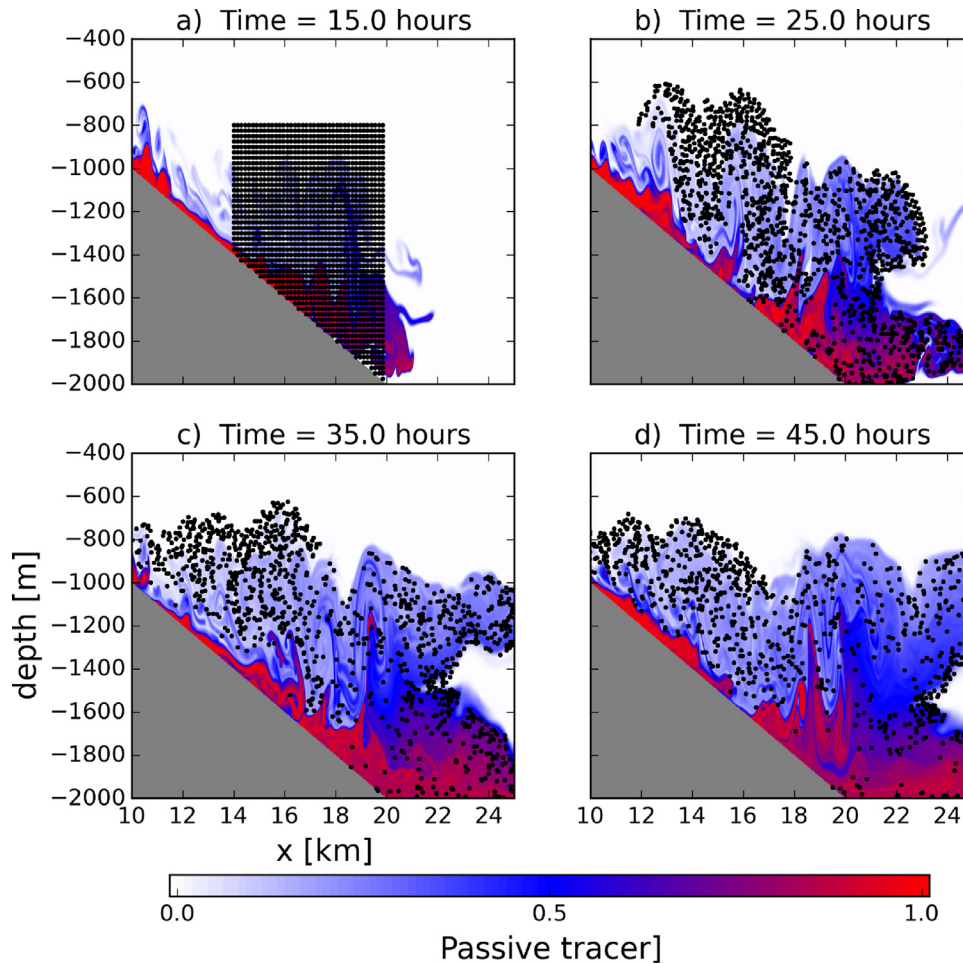


**Fig. 13.** Time evolution of 1444 particles advected between  $15 \text{ h} \leq t \leq 45 \text{ h}$  using the velocity field from an experiment where flow splitting occurs ( $\alpha = 0.1$ ,  $Pr = 50$  and  $B_0 = 0.016$ ). The particles were seeded at time = 15 hours and their time evolution reveals a slow counter-clockwise circulation on the top of the density current, between approximately  $10 \text{ km} \leq x \leq 18 \text{ km}$ . Snapshots of passive tracer distribution ( $\tau$ , color) are also plotted in the background. Corresponding animation is available in the auxiliary materials (ms10).

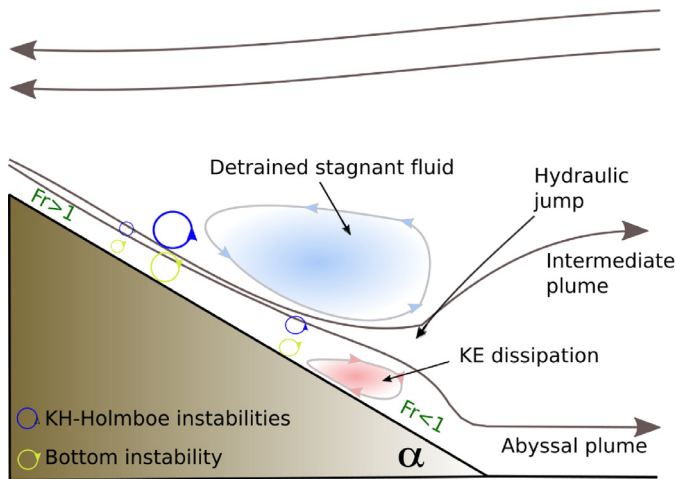


**Fig. 14.** Schematic depiction of the processes occurring in the flow splitting regime.

ence does not guarantee that flow splitting will occur. Instead, our results show that all the following characteristics are necessary for the development of flow splitting:  $B_0 \sim 10^{-2}$ ,  $R > 2$ , and the development of an internal hydraulic jump.

Recent laboratory studies (Cortés et al., 2014b) and numerical simulations (Cortés et al., 2015) of gravity currents encountering a density step in a two-layered stratified basin have stressed the importance of the internal properties in determining the behavior of the flow. It was shown that gravity currents are more likely to split as the density interface becomes more diffusive. That is, the flow is more likely to detrain into two parts as  $Fr$  increases (equivalent to  $Ri$  decreasing). Our numerical experiments show that, in a linearly stratified environment where the density current is initially supercritical ( $Fr > 1$ ), flow splitting is more likely to occur as  $Ri$  ( $Fr$ ) increases (decreases). This disparity is likely a direct consequence of the different types of instabilities that may occur in these systems.

#### 4.2. Application to oceanic outflows

We now compare  $\alpha$  versus  $Ri_0$  for all the numerical experiments conducted here (Fig. 15, see also Table 2 for a full list of all parameters). The experiments are separated into three groups, based on  $B_0$ , and the different flow regimes are plotted with different colors. Regardless of  $\alpha$  and  $Ri_0$ , when  $B_0 = 0.002$  the outflow always generates an underflow (Fig. 15a). Similarly, when  $B_0 = 0.13$ , the system always results in an interflow (Fig. 15c). However, when  $B_0 = 0.016$ , the type of regime is dictated by  $\alpha$  and  $Ri_0$  (Fig. 15b). For  $\alpha = 0.1$ , split flows occur when  $Ri_0 \geq 0.18$  and an interflow occurs otherwise. As the slope becomes shallower, the con-

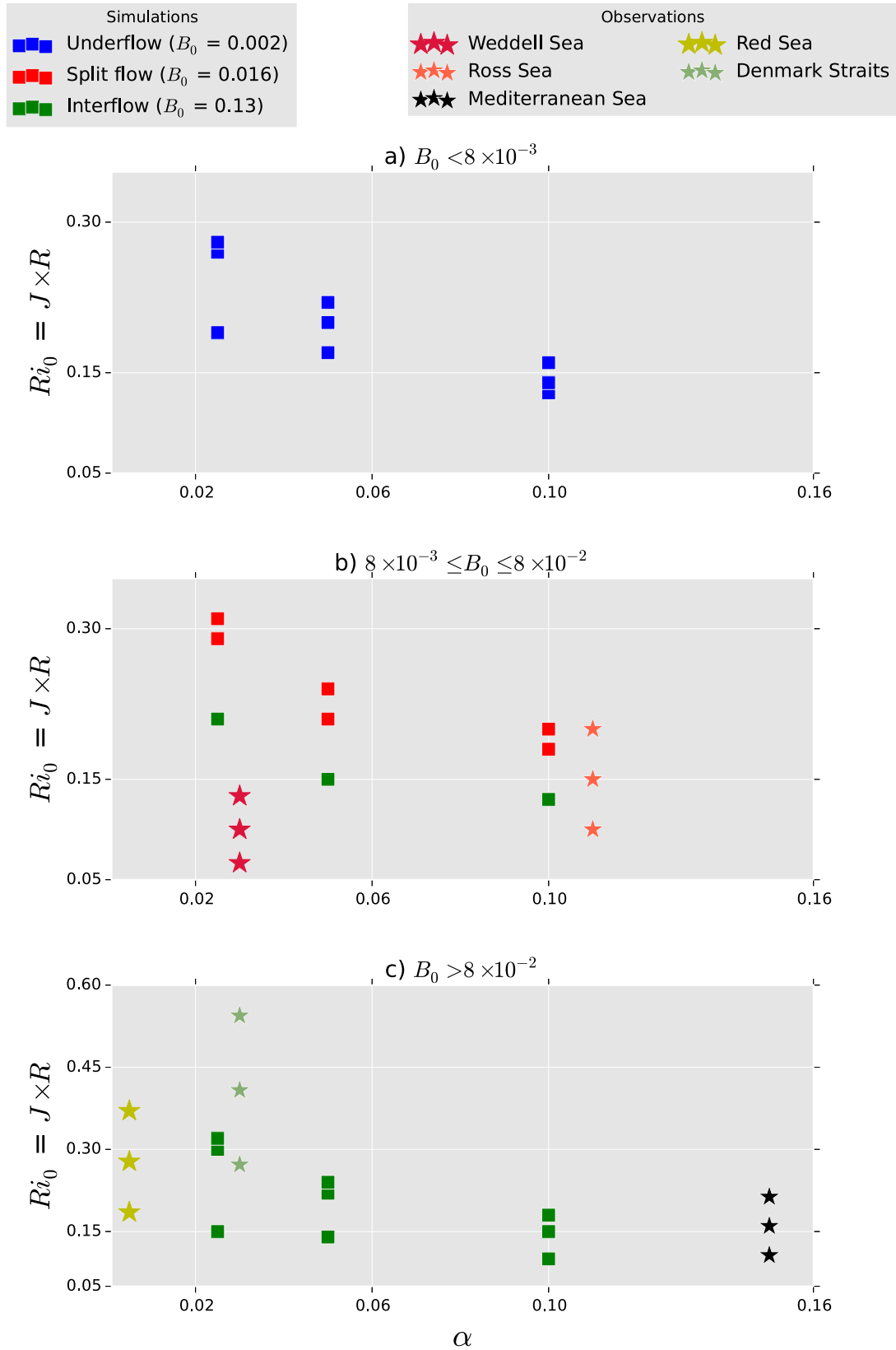


**Fig. 15.** Shelf slope ( $\alpha$ ) versus center Richardson number ( $Ri_0 = J \times R$ ) for all the simulations conducted here (see also Table 2). The results are divided into three groups based on the initial buoyancy number ( $B_0$ ): a)  $B_0 < 8.0 \times 10^{-3}$ ; b)  $8.0 \times 10^{-3} \leq B_0 \leq 8.0 \times 10^{-2}$ ; c)  $B_0 > 8.0 \times 10^{-2}$ . Simulated underflows, split flows and interflows, are represented by the blue, red and green squares, respectively. Also shown are the values for various oceanic outflows, representing the conditions at the top of the slope, inferred from available observations (stars, see Table 3 for additional information). (For interpretation of the references to colour in this figure legend, the reader is referred to the web version of this article.)

**Table 2**

Parameters for all numerical simulations conducted here (see text for the definition). The data is grouped based on  $Pr$ , with a)  $Pr = 1$ ; b)  $Pr = 10$ ; and c)  $Pr = 50$ .

	$Q_0$ ( $\text{m}^2 \text{ s}^{-1}$ )	$g'_0$ ( $\text{m s}^{-2}$ )	$N$ ( $\text{s}^{-1}$ )	$\alpha$	$B_0$	$R$	$Ri_0$	$Re_e$
a)	50.6	$1.8 \times 10^{-3}$	$5.0 \times 10^{-4}$	0.025	0.002	1.4	0.19	10.12
	50.4	$1.8 \times 10^{-3}$	$5.0 \times 10^{-4}$	0.05	0.002	1.3	0.17	10.08
	51.4	$1.8 \times 10^{-3}$	$5.0 \times 10^{-4}$	0.1	0.002	1.2	0.13	10.28
	47.8	$1.7 \times 10^{-3}$	$1.0 \times 10^{-3}$	0.025	0.016	1.6	0.21	9.56
	48.3	$1.7 \times 10^{-3}$	$1.0 \times 10^{-3}$	0.05	0.016	1.3	0.15	9.66
	48.2	$1.7 \times 10^{-3}$	$1.0 \times 10^{-3}$	0.1	0.016	1.2	0.13	9.64
	62.6	$2.7 \times 10^{-3}$	$2.5 \times 10^{-3}$	0.025	0.130	1.3	0.15	8.35
	62.1	$2.7 \times 10^{-3}$	$2.5 \times 10^{-3}$	0.05	0.130	1.2	0.14	8.28
	61.2	$2.7 \times 10^{-3}$	$2.5 \times 10^{-3}$	0.1	0.130	0.9	0.10	8.16
b)	51.2	$1.8 \times 10^{-3}$	$5.0 \times 10^{-4}$	0.025	0.002	2.3	0.27	10.24
	51.8	$1.8 \times 10^{-3}$	$5.0 \times 10^{-4}$	0.05	0.002	1.9	0.20	10.36
	50.7	$1.8 \times 10^{-3}$	$5.0 \times 10^{-4}$	0.1	0.002	1.8	0.14	10.14
	48.2	$1.7 \times 10^{-3}$	$1.0 \times 10^{-3}$	0.025	0.016	2.4	0.29	9.64
	48.0	$1.7 \times 10^{-3}$	$1.0 \times 10^{-3}$	0.05	0.016	2.1	0.21	9.60
	47.7	$1.7 \times 10^{-3}$	$1.0 \times 10^{-3}$	0.1	0.016	2.0	0.18	9.54
	62.5	$2.7 \times 10^{-3}$	$2.5 \times 10^{-3}$	0.025	0.130	2.3	0.30	8.33
	61.5	$2.7 \times 10^{-3}$	$2.5 \times 10^{-3}$	0.05	0.130	1.8	0.22	8.20
	61.2	$2.7 \times 10^{-3}$	$2.5 \times 10^{-3}$	0.1	0.137	1.8	0.15	8.16
c)	51.2	$1.8 \times 10^{-3}$	$5.0 \times 10^{-4}$	0.025	0.002	2.3	0.28	10.24
	51.8	$1.8 \times 10^{-3}$	$5.0 \times 10^{-4}$	0.05	0.002	2.2	0.22	10.36
	51.4	$1.8 \times 10^{-3}$	$5.0 \times 10^{-4}$	0.1	0.002	2.0	0.16	10.28
	48.5	$1.7 \times 10^{-3}$	$1.0 \times 10^{-3}$	0.025	0.016	2.7	0.31	9.70
	48.0	$1.7 \times 10^{-3}$	$1.0 \times 10^{-3}$	0.05	0.016	2.4	0.24	9.60
	48.1	$1.7 \times 10^{-3}$	$1.0 \times 10^{-3}$	0.1	0.016	2.3	0.20	9.62
	62.0	$2.7 \times 10^{-3}$	$2.5 \times 10^{-3}$	0.025	0.130	2.5	0.32	8.27
	62.6	$2.7 \times 10^{-3}$	$2.5 \times 10^{-3}$	0.05	0.130	2.2	0.24	8.35
	61.7	$2.7 \times 10^{-3}$	$2.5 \times 10^{-3}$	0.1	0.139	2.2	0.18	8.23

**Table 3**

Parameters representing the conditions at the top of the slope for selected oceanic outflows estimated based on the observations presented in the following articles: Ross Sea: [Gordon et al. \(2004\)](#), [Muench et al. \(2009\)](#); Mediterranean Sea: [Baringer and Price \(1997\)](#), [Price et al. \(1993\)](#); Weddell Sea: [Foldvik et al. \(2004\)](#); Denmark Straits: [Girton and Sanford \(2003\)](#); Red Sea: [Matt and Johns \(2007\)](#), [Peters et al. \(2005\)](#). The parameters for the two laboratory experiments conducted by [Baines \(2005\)](#) that resulted in flow splitting are also shown.

Region	$\alpha$	$g'_0$ ( $\text{m s}^{-2}$ )	$N$ ( $\text{s}^{-1}$ )	$h_0$ (m)	$U_0$ ( $\text{m s}^{-1}$ )	$Q_0$ ( $\text{m}^2 \text{ s}^{-1}$ )	$B_0$	$J$	$Re$
Ross Sea	0.11	$2 \times 10^{-3}$	$7.0 \times 10^{-4}$	150	1.0	150	$1.3 \times 10^{-2}$	0.10	$1.5 \times 10^8$
Med. Sea	0.15	$1.6 \times 10^{-3}$	$2.0 \times 10^{-3}$	200	1.0	200	$7.2 \times 10^{-1}$	0.11	$2.0 \times 10^8$
Red Sea	0.004	$1.4 \times 10^{-2}$	$7.0 \times 10^{-3}$	100	0.55	55	$9.6 \times 10^{-2}$	0.19	$5.5 \times 10^7$
Weddell Sea	0.03	$2 \times 10^{-3}$	$7.0 \times 10^{-4}$	100	1.0	100	$9.0 \times 10^{-3}$	0.07	$1.0 \times 10^8$
Denmark Straits	0.03	$2 \times 10^{-3}$	$1.3 \times 10^{-3}$	200	0.7	140	$7.7 \times 10^{-2}$	0.27	$1.4 \times 10^8$
Baines	0.72	25.01	1.22	0.27	2.27	0.61	$1.8 \times 10^{-3}$	1.13	61.4
Baines	0.72	22.65	1.16	0.61	2.16	1.32	$4.0 \times 10^{-3}$	2.55	132.0

ditional  $Ri_0$  required for flow splitting increases to 0.20 and 0.29, for  $\alpha = 0.05$  and 0.025, respectively.

For comparison, [Fig. 15](#) also shows the parameter values at the top of the slope (i.e., at the level of the initial outflow) inferred from observations of selected oceanic outflows (see [Table 3](#)). The  $B_0$  values derived from observations of oceanic outflows are between  $9.0 \times 10^{-3}$  and  $7.2 \times 10^{-1}$ , while  $\alpha$  varies between 0.03 and 0.15. The bulk Richardson number,  $J$ , was estimated by assuming  $\Delta U \sim U$ . Microstructure measurements of oceanic outflows are very rare and we could not infer  $h_u$  and  $R$  from the available observations. Therefore, estimates from observations are plotted by assuming  $h_u \sim h_0/3$  and three values of  $R$  (1, 1.5 and 2.0). Lastly, following [Baines \(2005\)](#), the Reynolds number is estimated as  $Re = \frac{Q_0}{\nu}$ , where  $\nu$  is the molecular viscosity ( $\nu = 1.0 \times 10^{-6} \text{ m}^2 \text{ s}^{-1}$ ).

The parameters estimated for the Ross Sea outflows (orange stars in [Fig. 15b](#)) fall in the range of  $B_0$  that, based on our numerical experiments, are propitious to either the interflow regime (when  $Ri_0 = 0.1$ ) or the flow splitting regime (when  $Ri_0 = 0.2$ );  $Ri_0 = 0.15$  falls between the two regimes, so it is not clear which regime occurs in this case. The parameters for the Denmark Straits,

Mediterranean, Weddell, and Red Seas fall within numerical experiments that result in the interflow regime ([Fig. 15c](#)). None of the estimates based on observations of oceanic outflows fall within numerical experiments that generate the underflow regime. This is unexpected since observations (see references in [Table 3](#)) show that the outflows from the Denmark Straits, Weddell and Ross Seas sink to the bottom of their respective ocean basins. It is possible that two factors that are likely to occur in oceanic outflows but are not considered in our analyses may contribute to the descent of these outflows. First, the parameters derived from observations shown in [Table 3](#) and [Fig. 15](#) represent the conditions at the top of the shelf slope and these are likely to vary significantly further downslope, potentially leading to transitions between different regimes. In particular, the ambient stratification ( $N$ ) in these outflows is likely to be significantly smaller at larger depths. Second, the thermobaric effect ([Gill, 1973](#); [Matsumura and Hasumi, 2010](#)) might be important in maintaining the density anomaly as the outflow reaches large depths.

[Fig. 15](#) does not include the results from the two laboratory experiments presented by [Baines \(2005, 2008\)](#) that generated split flows, since the parameter values in these experiments differ sig-

nificantly from the range investigated in our numerical simulations and observations; however, these values are listed in Table 3. To generate a turbulent flow (i.e., large enough  $Re$  values), the slope used in these experiments was much larger than those observed in nature and this is a general drawback of laboratory experiments of turbulent gravity currents. In addition, the ambient stratification frequency used in these experiments were at least two orders of magnitude larger than the typical values next to the major oceanic outflows (Table 3). Both parameters ( $\alpha$  and  $N$ ) are important in setting the conditions under which different turbulent regimes may occur. Therefore, we conclude that the flow regime criteria obtained in laboratory experiments of dense fluid down slope and into stratified environments differ from that obtained under geophysical parameters and scales. Based on our results and observations taken in the Ross and Weddell Seas, we hypothesize that flow splitting around Antarctica could carry water properties from the shelf into the deep ocean at two distinct depths.

#### 4.3. Influence of the maximum ocean depth

So far, the influence of the maximum ocean depth ( $H_{\max}$ ) on the development of the outflow has been ignored. Assuming conditions where an outflow would equilibrate at a depth  $H_e$  (i.e., become neutrally buoyant), a very deep ocean ( $H_{\max} \gg H_e$ ) would never result in an underflow. Similarly, a very shallow ocean ( $H_{\max} \ll H_e$ ) would never produce an interflow. It is therefore useful to quantify how the vertical distance between the top ( $H_{\text{shelf}}$ ) and bottom ( $H_{\max}$ ) of the slope ( $\Delta H = H_{\max} - H_{\text{shelf}}$ ) compares with the neutral buoyancy level ( $H_e = g_0/N^2$ ), relative to  $H_{\text{shelf}}$ , that the outflow would achieve in the absence of mixing. The relevant non-dimensional parameter,  $H^* = \Delta H/H_e$ , is expected to be small for underflows and large for interflows. In our numerical experiments, where  $\Delta H$  is always 1500 m,  $H^*$  is 0.21, 0.88 and 3.47 for cases where underflows, split flows and interflows are generated, respectively (i.e., when  $B_0 = 0.002, 0.016$  and  $0.13$ , respectively; see Table 3). Since we kept  $\Delta H$  constant, changing  $B_0$  by varying  $N$  and/or  $g_0$  is equivalent to changing  $H^*$ . However, it is possible to change  $H^*$  while keeping  $B_0$  fixed (i.e., by changing  $\Delta H$ ) and this could modify the flow regimes obtained based only on  $B_0$ . For example, it is possible that if we were to repeat the set of experiments where  $B_0 = 0.002$  using a larger  $\Delta H$  the flow would result in an interflow or a split flow rather than an underflow. Therefore, although we have not varied  $H_0$  in our set of experiments, the influence of this parameter should also be considered when inferring the flow regime of the system.

For the real oceanic outflows listed in Table 3,  $H^* \gg 1$  for the Mediterranean Sea, the Red Sea and the Denmark Straits outflows, suggesting interflows (where  $\Delta H \sim 3000, 1500, 3500$  m, respectively), while  $H^* \sim 0.63$  for the Ross Sea outflow ( $\Delta H \sim 2500$  m) and 0.88 for Weddell Sea outflow ( $\Delta H \sim 3500$  m), suggesting flow splitting. This classification is consistent with the regimes proposed based on  $B_0$ .

#### 4.4. Assumptions, limitations and recommendations for future studies

The results discussed thus far are all based on 2D simulations. In terms of turbulence, there is a fundamental difference between 2D and 3D, where energy cascades towards larger scales in the first and towards smaller scales in the latter (e.g., Vallis, 2006). Since one of the goals of this study is to investigate the conditions under which the flow splitting regime may occur in oceanic outflows, this distinction puts in doubt whether this regime can be generated in a 3D system. In the context of large-scale oceanic outflows, the numerical simulations conducted by Özgökmen et al. (2004) show that mixing in 2D simulations is overestimated when compared to the values obtained in laboratory experiments and in 3D simula-

tions. The authors attributed this difference to the absence of secondary instabilities in 2D, while in 3D such instabilities develop in the along-slope direction and lead to a rapid breakdown of the vortices. Numerical simulations of gravity-current fronts in the lock-exchange configuration also revealed that vortices in 2D are unable to break down as they do in 3D, which therefore affects mixing and the density field (Härtel et al., 2000). Although it is likely that flow splitting will also occur in 3D simulations, we anticipate that in fully 3D systems the transition from one regime to another and the correspondent value of  $B_0$  for each regime may differ from those presented here.

In addition to three-dimensionality, most oceanic outflows are also strongly influenced by rotation. For unconstrained flows going down broad slopes, which is the case of our simulations, rotation will balance the downward flow and therefore result in a large portion of the dense fluid following  $f/H$  contours, where  $f$  is the Coriolis parameter and  $H$  is the total water depth. In this case, an additional flow regime where the plume is arrested can also occur (Wobus et al., 2013). In terms of mixing, the rotating experiments of unconstrained flows reported by Wells (2007) show entrainment rates similar to those obtained in similar non-rotating experiments reported by Ellison and Turner (1959). However, in the presence of vertical walls or inclined boundaries, e.g., ridges or canyons, secondary flows induced by rotation lead to more vigorous entrainment than in non-rotating systems. Topographic features are often present along continental slopes around the oceans, including regions of major oceanic outflows (e.g., see Fig. 1 in Allen and Durrieu de Madron, 2009). Since submarine canyons and ridges increase entrainment rates (Wählin et al., 2008), the transition  $B_0$  values for the different flow regimes are likely to differ from those presented here. Therefore, future research should consider the effects of both rotation and three-dimensionality, ideally in the presence of small-scale topographic features, to confirm if the outcomes of this study are still valid under such conditions.

The low effective Reynolds number ( $Re_e = Q_0/\nu_h$ ) values of the outflow in our numerical experiments (see Table 2) are also a limitation that needs to be addressed. Although these values are similar (i.e., same order of magnitude) to the  $Re$  values obtained in the laboratory experiment conducted by Baines (2005, 2008), they are much smaller than  $Re$  values observed next to the major oceanic outflows (Table 3). Thus, future numerical studies are required to confirm if the outcomes of this study also hold under larger effective Reynolds number. This will require the application of direct numerical simulations (DNS), where all scales of motion down to the Kolmogorov scale are explicitly resolved (i.e., without any turbulence closure). Although this method is computationally very expensive (even for a 2D setup similar to the one employed here), the results presented here can be used as a guide to narrow the parameter space to be explored.

Finally, in all simulations conducted here, the outflow is initially supercritical ( $Fr > 1$ ) since most oceanic outflows fall in this category (Legg et al., 2009). To simulate subcritical conditions following our choice of parameters and scales would require much higher vertical resolution, since subcritical outflows, in general, tend to develop step-like velocity and density profiles (e.g., Cortés et al., 2014b). Hence, whether the outcomes of this study apply to subcritical conditions remains to be tested. Nevertheless, we do not expect that the flow splitting regime will occur in subcritical outflows since internal hydraulic jumps are not likely to develop in such conditions.

## 5. Concluding remarks

A comparison between our numerical results and oceanic observations suggests that flow splitting may occur in dense-water outflows with weak ambient stratification, such as Antarctic outflows.

Oceanic outflows, in general, are not well represented in the current generation of climate models and this is one of the main challenges for improving climate predictions (e.g., Heuzé et al., 2013; Legg et al., 2009). Therefore, it would be extremely valuable to confirm whether flow splitting occurs in these systems. The outcomes of the present study can be used in the design of observational programs that aim to study oceanic outflows, as well as in future numerical and laboratory studies. Perhaps the best way to observe flow splitting in these systems would involve the release of some kind of tracer (e.g., rhodamine) into the dense water before it flows downslope. Although this procedure may not be feasible in large-scale outflows, given the extremely large amount of dye that would be required and the long time needed to observe its offshore response, a dye release into a smaller scale system such as a fjord overflow would be much more feasible. Anthropogenic tracers, such as radionuclide and chlorofluorocarbons, may provide a possible alternative to detect flow splitting in large-scale outflows.

Finestructure and microstructure measurements of velocity and buoyancy profiles within outflows would provide valuable support for the processes suggested by our simulations. This information can then be used, in combination with other environmental parameters (i.e., ambient stratification and bottom slope), to identify the flow regimes based on the results presented here. However, such comparison must be performed with caution since three-dimensionality and rotation (both absent in our simulations) will affect mixing and, therefore, the values representing the transition from each flow regime are likely to differ from those obtained based on our numerical experiments. In addition, the parameters governing the flow regimes are expected to vary downstream of the initial level of the outflow, perhaps leading to a transition between different flow regimes.

Lastly, for simplicity and lack of knowledge on what value  $Pr$  takes in real oceanic outflows, numerical studies often assume  $Pr = 1$  (Özgökmen et al., 2004, 2006; Özgökmen and Fischer, 2008; Wobus et al., 2013). Our study demonstrates that flow splitting occurs when  $Pr \geq 10$  and this highlights the need to further investigate the actual form of  $Pr$  in oceanic outflows so that appropriate values can be used in numerical models.

## Acknowledgments

This research was partially supported by the National Science Foundation grants OCE-0961369 and OCE-0961405. We thank Larry J. Pratt, Anirban Guha, Andy Hogg and Dustin Carroll for many helpful discussions during the development of this manuscript. Comments from Sonya Legg, Steve Griffies and two anonymous reviewers helped to improve the manuscript. Computer time was made available by the ocean group at GFDL.

## Supplementary material

Supplementary material associated with this article can be found, in the online version, at [10.1016/j.ocemod.2017.03.011](https://doi.org/10.1016/j.ocemod.2017.03.011)

## References

- Aagaard, K., Swift, J., Carmack, E., 1985. Thermohaline circulation in the Arctic Mediterranean seas. *J. Geophys. Res.* 90 (C3), 4833–4846.
- Adcroft, A., Hill, C., Marshall, J., 1997. Representation of topography by shaved cells in a height coordinate ocean model. *Mon. Weather Rev.* 125 (9), 2293–2315.
- Allen, S., Durrieu de Madron, X., 2009. A review of the role of submarine canyons in deep-ocean exchange with the shelf. *Ocean Sci.* 5 (4), 607–620.
- Baines, P.G., 2001. Mixing in flows down gentle slopes into stratified environments. *J. Fluid Mech.* 443, 237–270.
- Baines, P.G., 2005. Mixing regimes for the flow of dense fluid down slopes into stratified environments. *J. Fluid Mech.* 538, 245–267.
- Baines, P.G., 2008. Mixing in downslope flows in the ocean—plumes versus gravity currents. *Atmos. Ocean* 46 (4), 405–419.
- Baringer, M., Price, J., 1997. Mixing and spreading of the mediterranean outflow. *J. Phys. Oceanogr.* 27 (8), 1654–1677.
- Cenedese, C., Adduce, C., 2008. Mixing in a density-driven current flowing down a slope in a rotating fluid. *J. Fluid Mech.* 604, 369–388.
- Cenedese, C., Whitehead, J.A., Ascarelli, T., Ohiwa, M., 2004. A dense current flowing down a sloping bottom in a rotating fluid. *J. Phys. Oceanogr.* 34 (1), 188–203.
- Cortés, A., Fleenor, W.E., Wells, M.G., de Vicente, I., Rueda, F.J., 2014. Pathways of river water to the surface layers of stratified reservoirs. *Limnol. Oceanogr.* 59 (1), 233–250.
- Cortés, A., Rueda, F.J., Wells, M.G., 2014. Experimental observations of the splitting of a gravity current at a density step in a stratified water body. *J. Geophys. Res.* 119 (2), 1038–1053.
- Cortés, A., Wells, M.G., Fringer, O.B., Arthur, R., Rueda, F.J., 2015. Numerical investigation of split flows by gravity currents into two-layered stratified water bodies. *J. Geophys. Res.* 120 (7), 5254–5271.
- De Cesare, G., Boillat, J.-L., Schleiss, A.J., 2006. Circulation in stratified lakes due to flood-induced turbidity currents. *J. Environ. Eng.* 132 (11), 1508–1517.
- Elliott, Z.A., Venayagamoorthy, S.K., 2011. Evaluation of turbulent Prandtl (Schmidt) number parameterizations for stably stratified environmental flows. *Dyn. Atmos. Oceans* 51 (3), 137–150.
- Ellison, T.H., Turner, J.S., 1959. Turbulent entrainment in stratified flows. *J. Fluid Mech.* 6 (03), 423–448.
- Ezer, T., 2005. Entrainment, diapycnal mixing and transport in three-dimensional bottom gravity current simulations using the Mellor–Yamada turbulence scheme. *Ocean Modell.* 9 (2), 151–168.
- Foldvik, A., Gammelsrød, T., Østerhus, S., Fahrbach, E., Rohardt, G., Schröder, M., Nicholls, K.W., Padman, L., Woodgate, R.A., 2004. Ice shelf water overflow and bottom water formation in the southern Weddell sea. *J. Geophys. Res.* 109 (C2), 1–15.
- Gill, A., 1973. Circulation and bottom water production in the Weddell sea. *Deep. Sea. Res.* 20, 111–140.
- Girton, J.B., Sanford, T.B., 2003. Descent and modification of the overflow plume in the Denmark strait\*. *J. Phys. Oceanogr.* 33 (7), 1351–1364.
- Gordon, A.L., Zambianchi, E., Orsi, A., Visbeck, M., Giulivi, C.F., Whitworth III, T., Spezie, G., 2004. Energetic plumes over the western Ross Sea continental slope. *Geophys. Res. Lett.* 31, L21302, doi: 10.1029/2004GL020785
- Griffies, S.M., Pacanowski, R.C., Hallberg, R.W., 2000. Spurious diapycnal mixing associated with advection in a z-coordinate ocean model. *Mon. Weather Rev.* 128 (3), 538–564.
- Guo, Y., Zhang, Z., Shi, B., 2014. Numerical simulation of gravity current descending a slope into a linearly stratified environment. *J. Hydraulic Eng.* 140 (12), 04014061.
- Härtel, C., Meiburg, E., Necker, F., 2000. Analysis and direct numerical simulation of the flow at a gravity-current head. part 1. flow topology and front speed for slip and no-slip boundaries. *J. Fluid Mech.* 418, 189–212.
- Heuzé, C., Heywood, K.J., Stevens, D.P., Ridley, J.K., 2013. Southern ocean bottom water characteristics in CMIP5 models. *Geophys. Res. Letters* 40 (7), 1409–1414.
- Hogg, A.M., Ivey, G., 2003. The Kelvin–Helmholtz to Holmboe instability transition in stratified exchange flows. *J. Fluid Mech.* 477, 339–362.
- Holland, D.M., Rosales, R.R., Stefanica, D., Tabak, E.G., 2002. Internal hydraulic jumps and mixing in two-layer flows. *J. Fluid Mech.* 470, 63–83.
- Howard, L.N., 1961. Note on a paper of John W. Miles. *J. Fluid Mech.* 10 (04), 509–512.
- Hughes, G., Griffiths, R., 2006. A simple convective model of the global overturning circulation, including effects of entrainment into sinking regions. *Ocean Modell.* 12 (1), 46–79.
- Ilicak, M., Adcroft, A.J., Griffies, S.M., Hallberg, R.W., 2012. Spurious diapycnal mixing and the role of momentum closure. *Ocean Modell.* 45–46, 37–58.
- Jackson, L., Hallberg, R., Legg, S., 2008. A parameterization of shear-driven turbulence for ocean climate models. *J. Phys. Oceanogr.* 38 (5), 1033–1053.
- Lane-Serff, G., Baines, P., 1998. Eddy formation by dense flows on slopes in a rotating fluid. *J. Fluid Mech.* 363, 229–252.
- Legg, S., Ezer, T., Jackson, L., Briegleb, B., Danabasoglu, G., Large, W., Wu, W., Chang, Y., Özgökmen, T.M., Peters, H., Xu, X., Chassignet, E.P., Gordon, A.L., Griffies, S., Hallberg, R., Price, J., Riemenschneider, U., Yang, J., 2009. Improving oceanic overflow representation in climate models: the gravity current entrainment climate process team. *Bull. Am. Meteorol. Soc.* 90 (5), 657–670.
- Legg, S., Hallberg, R., Girton, J., 2006. Comparison of entrainment in overflows simulated by -coordinate, isopycnal and non-hydrostatic models. *Ocean Modell.* 11 (1–2), 69–97.
- Legg, S., Klymak, J., 2008. Internal hydraulic jumps and overturning generated by tidal flow over a tall steep ridge. *J. Phys. Oceanogr.* 38 (9), 1949–1964.
- Long, R.R., 1953. Some aspects of the flow of stratified fluids: i. a theoretical investigation. *Tellus* 5 (1), 42–58.
- Long, R.R., 1954. Some aspects of the flow of stratified fluids: II. experiments with a two-fluid system. *Tellus* 6 (2), 97–115.
- Marques, G.M., Özgökmen, T.M., 2014. On modeling turbulent exchange in buoyancy-driven fronts. *Ocean Modell.* 83, 43–62.
- Marshall, J., Adcroft, A., Hill, C., Perelman, L., Heisey, C., 1997. A finite-volume, incompressible Navier–Stokes model for studies of the ocean on parallel computers. *J. Geophys. Res.* 102 (C3), 5753–5766.
- Marshall, J., Hill, C., Perelman, L., Adcroft, A., 1997. Hydrostatic, quasi-hydrostatic, and nonhydrostatic ocean modeling. *J. Geophys. Res.* 102 (C3), 5733–5752.
- Matsumura, Y., Hasumi, H., 2010. Modeling ice shelf water overflow and bottom water formation in the southern Weddell sea. *J. Geophys. Res.* 115 (C10), 1–17.

- Matt, S., Johns, W.E., 2007. Transport and entrainment in the Red Sea outflow plume. *J. Phys. Oceanogr.* 37 (4), 819–836.
- Mauritzen, C., Price, J., Sanford, T., Torres, D., 2005. Circulation and mixing in the Faroese channels. *Deep Sea Res. I* 52 (6), 883–913.
- McDougall, T.J., 1987. Thermobaricity, cabbelling, and water-mass conversion. *J. Geophys. Res.* 92 (C5), 5448–5464.
- Miles, J.W., 1961. On the stability of heterogeneous shear flows. *J. Fluid Mech.* 10 (04), 496–508.
- Mitsudera, H., Baines, P.G., 1992. Downslope gravity currents in a continuously stratified environment: a model of the bass strait outflow. In: 11th Australasian Fluid Mechanics Conf., pp. 1017–1020.
- Monaghan, J.J., 2007. Gravity current interaction with interfaces. *Annu. Rev. Fluid Mech.* 39, 245–261.
- Muench, R., Padman, L., Gordon, A., Orsi, A., 2009. A dense water outflow from the Ross Sea, Antarctica: Mixing and the contribution of tides. *J. Mar. Sys.* 77 (4), 369–387.
- Necker, F., Härtel, C., Kleiser, L., Meiburg, E., 2002. High-resolution simulations of particle-driven gravity currents. *Int. J. Multiphase Flow* 28 (2), 279–300.
- Özgökmen, T.M., Chassignet, E.P., 2002. Dynamics of two-dimensional turbulent bottom gravity currents. *J. Phys. Oceanogr.* 32 (5), 1460–1478.
- Özgökmen, T.M., Fischer, P.F., 2008. On the role of bottom roughness in overflows. *Ocean Modell.* 20 (4), 336–361.
- Özgökmen, T.M., Fischer, P.F., Duan, J., Iliescu, T., 2004. Three-dimensional turbulent bottom density currents from a high-order nonhydrostatic spectral element model. *J. Phys. Oceanogr.* 34 (9), 2006–2026.
- Özgökmen, T.M., Fischer, P.F., Johns, W.E., 2006. Product water mass formation by turbulent density currents from a high-order nonhydrostatic spectral element model. *Ocean Modell.* 12 (3), 237–267.
- Padman, L., Howard, S.L., Orsi, A.H., Muench, R.D., 2009. Tides of the northwestern ross sea and their impact on dense outflows of Antarctic bottom water. *Deep Sea Res. I* 56 (13–14), 818–834.
- Peters, H., Johns, W.E., Bower, A.S., Fratantoni, D.M., 2005. Mixing and entrainment in the Red Sea outflow plume. Part I: Plume structure. *J. Phys. Oceanogr.* 35 (5), 569–583.
- Pratt, L.J., Riemenschneider, U., Helfrich, K.R., 2007. A transverse hydraulic jump in a model of the Faroe Bank Channel outflow. *Ocean Modell.* 19 (1), 1–9.
- Price, J., Baringer, M., 1994. Outflows and deep water production by marginal seas. *Progr. in Oceanogr.* 33, 161–200.
- Price, J.F., Baringer, M.O., Lueck, R.G., Johnson, G.C., Ambar, I., Parrilla, G., Cantos, A., Kennelly, M.A., Sanford, T.B., 1993. Mediterranean outflow mixing and dynamics. *Science* 259 (5099), 1277–1282.
- Simpson, J.E., 1999. Gravity currents: In the environment and the laboratory. Cambridge University Press.
- Smyth, W., Carpenter, J., Lawrence, G., 2007. Mixing in symmetric holmboe waves. *J. Phys. Oceanogr.* 37 (6), 1566–1583.
- Smyth, W., Winters, K., 2003. Turbulence and mixing in holmboe waves. *J. Phys. Oceanogr.* 33 (4), 694–711.
- Strang, E., Fernando, H., 2001. Vertical mixing and transports through a stratified shear layer. *J. Phys. Oceanogr.* 31 (8), 2026–2048.
- Vallis, G.K., 2006. Atmospheric and oceanic fluid dynamics: fundamentals and large-scale circulation. Cambridge University Press.
- Wählin, A., Cenedese, C., 2006. How entraining density currents influence the stratification in a one-dimensional ocean basin. *Deep Sea Res. II* 53 (1), 172–193.
- Wählin, A., Darelius, E., Cenedese, C., Lane-Serff, G., 2008. Laboratory observations of enhanced entrainment in dense overflows in the presence of submarine canyons and ridges. *Deep Sea Res. I* 55 (6), 737–750.
- Wells, M., 2007. Influence of coriolis forces on turbidity currents and sediment deposition. In: Particle-Laden Flow. Springer, pp. 331–343.
- Wells, M., Nadarajah, P., 2009. The intrusion depth of density currents flowing into stratified water bodies. *J. Phys. Oceanogr.* 39 (8), 1935–1947.
- Wells, M.G., Wettlaufer, J.S., 2007. The long-term circulation driven by density currents in a two-layer stratified basin. *J. Fluid Mech.* 572, 37–58.
- Winton, M., Hallberg, R., Gnanadesikan, A., 1998. Simulation of density-driven frictional downslope flow in z-coordinate ocean models. *J. Phys. Oceanogr.* 28 (11), 2163–2174.
- Wobus, F., Shapiro, G.I., Huthnance, J.M., Maqueda, M.A.M., 2013. The piercing of the Atlantic layer by an Arctic shelf water cascade in an idealised study inspired by the Storfjorden overflow in Svalbard. *Ocean Modell.* 71, 54–65.